A SITELLE view of M31's central region – I. Calibrations and radial velocity catalogue of nearly 800 emission-line point-like sources

Thomas Martin, Laurent Drissen, Anne-Laure Melchior

HAL Id: hal-02303448

https://hal.science/hal-02303448

Submitted on 22 Feb 2023

A SITELLE view of M31's central region – I. Calibrations and radial velocity catalogue of nearly 800 emission-line point-like sources

Thomas B. Martin,[1,2]★ Laurent Drissen[1,2,3] and Anne-Laure Melchior[4]

[1]*Département de physique, de génie physique et d'optique, Université Laval, 2325, rue de l'université, Québec, ON G1V 0A6, Canada*
[2]*Centre de recherche en astrophysique du Québec, Département de physique, Université de Montréal C.P. 6128, Succ. Centre-Ville Montréal, QC Canada H3C 3J7*
[3]*Department of Physics and Astronomy, University of Hawai'i at Hilo, Hilo, HI 96720, USA*
[4]*LERMA, Sorbonne Universités, UPMC Univ. Paris 6, Observatoire de Paris, PSL Research University, CNRS, F-75000 Paris, France*

ABSTRACT

We present a detailed description of the wavelength, astrometric and photometric calibration plan for SITELLE, the imaging Fourier transform spectrometer attached to the Canada–France–Hawaii telescope, based on observations of a red (647–685 nm) data cube of the central region (11 arcmin × 11 arcmin) of M 31. The first application, presented in this paper is a radial-velocity catalogue (with uncertainties of ∼2–6 km s^{-1}) of nearly 800 emission-line point-like sources, including ∼450 new discoveries. Most of the sources are likely planetary nebulae, although we also detect five novae (having erupted in the first eight months of 2016) and one new supernova remnant candidate.

Key words: instrumentation: interferometers – methods: data analysis – techniques: imaging spectroscopy – planetary nebulae: general – galaxies: individual: M31 – galaxies: kinematics and dynamics.

1 INTRODUCTION

Aiming at characterizing the nearest low-ionization nuclear emission-line region, at the core of M 31, by studying line ratios and kinematics of the diffuse gas surrounding it (Melchior et al., in preparation), we have obtained a medium resolution ($R \sim 5000$) data cube in the H α–[N II]–[S II] range (649–684 nm) of a large section around the galaxy nucleus with the imaging Fourier transform spectrometer SITELLE.

This instrument, described in Baril et al. (2016), Drissen et al. (2010), Grandmont et al. (2012) and Drissen et al. (in preparation), consists of a Michelson interferometer inserted into the collimated beam of an astronomical camera system, equipped with two fast-readout, low-noise, deep depletion e2v CCD detectors (2048 × 2048, 0.32 arcsec pixels) providing a total field of view (FOV) of 11 arcmin × 11 arcmin. The spectral range of a given data cube is selected by inserting the desired filter, chosen from a list covering the entire visible range, from 350 to 850 nm, in front of the collimator. SITELLE's spectral resolution is very flexible, ranging from $R = 1$ (panchromatic) to $R = 20\,000$. Details on data acquisition, and the process of transforming the two initial interferometric cubes into a single, calibrated spectral cube, are presented below.

The detection of several hundred H α-emitting point sources in our M31 cube, some of which being new discoveries, has motivated the creation of a catalogue and, for this purpose, a

significant improvement of the calibration methods used for SITELLE's first data release (Martin & Drissen 2016, Martin et al., in preparation).

After a brief description of the instrument and the observations, Section 2 of this paper describes in detail the wavelength, astrometric and flux calibration of SITELLE data. Section 3 presents the method used to detect the H α-emitting point sources before introducing the catalogue and a comparison with previous work based on narrow-band imagery and multi-object dispersive spectroscopy.

2 OBSERVATIONS AND DATA CALIBRATION

2.1 Observations

The data cube was obtained on 2016 August 24, with SITELLE attached to the Canada–France–Hawaii telescope, and the SN3 filter (647–685 nm), designed to detect the H α line as well as the [N II] 6548, 6584 and [S II] 6717,6731 doublets in Milky Way H II regions and nearby galaxies up to $z = 0.017$. Parameters of the observations are listed in Table 1. The duration of the cube was 4.1 h, including the 3.8 s overhead per step (CCD readout and mirror displacement and stabilization) giving a total on-source exposure time of 3.2 h; sky was photometric and the median seeing, 0.9 arcsec, was well sampled by the 0.32 arcsec CCDs attached to both output ports of the interferometer. The target resolution was 5000 on the interferometer axis giving a resolution of 4900 at the centre of the FOV (at an incident angle of 15°.4). As we have not measured emission lines with a broadening significantly smaller than ∼20 km s^{-1}, we

★ E-mail: thomas.martin.1@ulaval.ca

the FTS technique[1] (Drissen et al. 2012, 2014; Maillard et al. 2013), combined with the short exposure time per step, strongly reduces the SNR and prevents any precise ($\leq 2 \, \mathrm{km \, s^{-1}}$) measurement of the sky lines centroid in the centre of the FOV. Nevertheless, on the border of the FOV, the level of continuum is low enough to provide accurate measurements of the sky lines velocity (see Fig. 4). Since the wavelength calibration is strongly tied to the optical structure of the interferometer, we can model the wavelength calibration map from a small set of instrumental parameters and fit the known velocity points (i.e. on the border of the FOV) to estimate the velocity where no reliable measure of the sky lines can be made (i.e. at the centre FOV). It is then possible to compute the correct wavelength calibration everywhere in the FOV with precision.

This improved calibration method involves the following:

(i) computation of a set of initial parameters from the calibration laser map measured at zenith;

(ii) measurement of the velocity of the sky lines, which translates directly into a wavelength calibration error since this velocity must be 0;

(iii) modelling of a new calibration laser map with a new set of parameters that fit the measured velocity of the sky lines.

We will now describe the model of the calibration laser map we have developed to relate the deformation of the optical structure to the value of the incident angle at each pixel of the FOV. Note that the calibration laser map is taken at zenith. The fit of this calibration laser map with the model permits to define an initial set of parameters which can eventually be changed to model what would be the real calibration laser map in the direction of the target (here M 31).

2.2.2 Calibration laser map modelling

The best way to fit a calibration laser map is to construct a model M defined as a function of instrumental parameters p, which permits to calculate σ, the measured laser wavenumber related to the wavelength λ via $\sigma = 1/\lambda$, at any given pixel position (x, y),

$$\sigma(x, y) = M(x, y, p). \tag{1}$$

Recalling that the angle between the interferometer axis and the detector pixel is θ, we can start by providing the relation between the measured velocity error ϵ_v and the error ϵ_θ made on the calculated value of the incident angle θ. Indeed, following equation (A6), any error on θ translates into an error on the measured wavenumber, σ, with respect to the real wavenumber σ_0,

$$\sigma = \frac{\sigma_0}{\cos(\theta + \epsilon_\theta)}. \tag{2}$$

This error will in turn result in an error on the measured velocity,

$$\epsilon_v = c \left(\frac{1}{\cos(\theta + \epsilon_\theta)} - \frac{1}{\cos(\theta)} \right), \tag{3}$$

where c is the speed of light.

---

[1] The multiplex disadvantage comes from the fact that all the photons of the interferogram ($\sim N$ photons per exposure $\times$ M exposures) are used to compute each spectral sample leading to a photon noise on each of the M spectral channels equal to the photon noise coming from $N \times M$ photons (i.e. $\sqrt{N \times M}$). If a dispersive technique was used to acquire the exact same spectrum with the same exposure time on a continuum source (e.g. a star emitting N photons per channel) the photon noise per channel would be $\sim \sqrt{N}$ i.e. $\sqrt{M}$ time better than the FTS technique. Note that this disadvantage is largely reduced if the source is monochromatic.

If the optics in front of the detector is not taken into account, i.e. the computed distances are not corrected for the optical magnification, an idealized structural model can be deduced from simple geometrical considerations (the optics and the detector are also considered distortion free). The detector is considered as a perfect plane perpendicular to the direction of the incoming beam at a distance d from the beamsplitter. Projected into spherical coordinates, as shown in Fig. 2, this angle is defined by its longitude λ and its latitude φ. The angles that define the direction from the origin to the centre of the detector (the detector axis) are λ_c and φ_c.

To calculate the incident angle of any pixel on the detector, one can first determine the angles $\Delta\lambda$ and $\Delta\varphi$ of this pixel with respect to the detector axis (the direction that points from the origin to the centre of the detector). Since the physical size of the pixel p is known (15 μm), the physical position of a pixel on the detector (x, y) can be simply related to its index (i_x, i_y)

$$x = p \, i_x \tag{4}$$

$$y = p \, i_y. \tag{5}$$

The rotation of the detector by an angle γ can be taken into account with a rotation matrix

$$x = p \, i_x \cos(\gamma) + p \, i_y \sin(\gamma) \tag{6}$$

$$y = p \, i_y \cos(\gamma) - p \, i_x \sin(\gamma). \tag{7}$$

The plane of the detector can also be tilted with respect to the plane perpendicular to the detector axis (tip-tilt angles α and β). The angle $\Delta\lambda$ and $\Delta\varphi$ are computed with the classical tangent law

$$\Delta\lambda = \arctan\left(\frac{x - d}{x + d} \frac{1}{\tan(0.5(\alpha + \pi/2))} \right) - \frac{\alpha}{2} + \frac{\pi}{4} \tag{8}$$

$$\Delta\varphi = \arctan\left(\frac{y - d}{y + d} \frac{1}{\tan(0.5(\beta + \pi/2))} \right) - \frac{\beta}{2} + \frac{\pi}{4}. \tag{9}$$

The direction of the pixel with respect to the interferometer axis is thus

$$\lambda = \lambda_c + \Delta\lambda \tag{10}$$

$$\varphi = \varphi_c + \Delta\varphi \tag{11}$$

and the incident angle θ can finally be derived with Vincenty's formula (Vincenty 1975),

$$\theta = \arctan\left(\frac{\sqrt{(\cos(\varphi)\sin(\lambda))^2 + \sin(\varphi)^2}}{\cos(\varphi)\cos(\lambda)} \right). \tag{12}$$

Finally, from equation (A2), we can compute the measured wavenumber of the laser source of nominal wavenumber σ_0 at a given incident angle θ (we recall the equation here for clarity)

$$\sigma_\theta = \sigma_0 \cos(\theta). \tag{13}$$

This model provides a good description of the measurement of the incident angle that can be done via the observation of a calibrated laser source. If we look at the typical values of the parameters returned by a fit of an arbitrary calibration laser map, we find a distance d of $\sim$23.5 cm (depending on the chosen wavelength of the calibration laser), which, magnified by 3.3 (the magnification of the camera optics), gives a real distance of $\sim$76 cm: a few centimetres
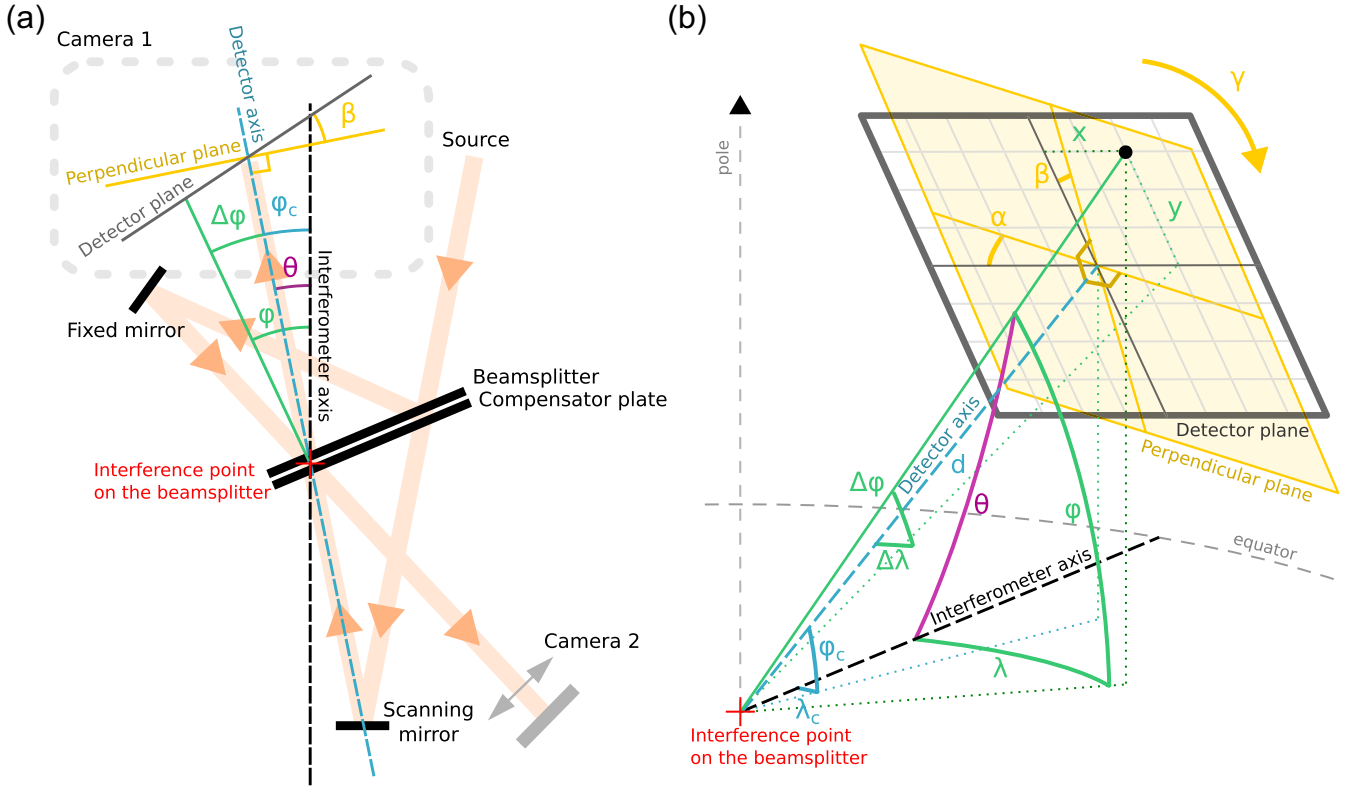
Figure 2. Idealized model of the interferometer structure. (a) 2D projection of the whole interferometer structure. The off-axis configuration, with a beamsplitter tilted with respect to the classical 45° configuration, appears clearly. Some of the indications shown in the complete 3D figure (b) are reported. The nominal incident angle θ at the centre of the detector is 15°.5. By projection the angles θ and φ seem to be the same but they are not. Note that the optics of the cameras, in front of the detector plane, is not taken into account in the model. (b) 3D representation of the model of the interferometer. The equator plane (or reference plane) and the pole direction of the spherical coordinates system are indicated in grey. The origin is the point on the beamsplitter where the detector axis crosses the semitransparent coating.

larger than the real distance from the dielectric coating to the detector surface. Tip-tilt angles are also generally small which appears mechanically correct.

However, this model does not take into account the distortions produced by the optics which slightly changes the position where the light at a given incident angle is measured on the detector (see Fig. 3).

If we assume that our model is correct in first approximation, the residual from the fit on the measured calibration laser map must come from optical aberrations, such as distortions and wavefront errors, with some normally distributed noise, $\mathcal{N}$, that can be reduced by fitting the residual with an appropriate model (Zernike polynomials in this case), i.e. from equation (1):

$$\sigma_{\text{observed}}(x, y) = M(x, y, p) + \text{DIR}(x, y) + \mathcal{N}, \qquad (14)$$

DIR(x, y) being the Distortion Induced Residual, as the optical distortions are a major contributor to this residual. Indeed, we can use the distortion model obtained from the astrometric calibration (see Section 2.3) and try to model what would be the observed DIR (see Fig. 3). We can see that, even if small features are not perfectly reproduced, most of the measured DIR can be explained by optical distortions, especially in the corners. Note also that we are using a distortion model calculated in the red part of the spectrum (the SN3 filter is centred at 666 nm) while the calibration laser map is observed at 543.5 nm and that distortions are likely to be chromatic.

A more careful study of the relation between the residual and the astrometric distortion pattern still needs to be done but is beyond the scope of this paper.

The idea that a complete model of the calibration map is the sum of a geometrical model of the interferometer that changes with the direction of the gravity vector plus a constant DIR (see equation 14) is confirmed by the comparison of the DIRs computed from the fit of five calibration laser maps obtained at different telescope pointings. During the commissioning, four calibration laser maps have been obtained at an angle of 47° in four different directions (north, south, east and west). They have been compared with a calibration laser map obtained at zenith. We have found that the difference between the DIRs computed with the fit of each of these five calibration laser maps was always smaller than $1 \, \text{km s}^{-1}$. However, the difference between the geometrical models $M(x, y, p)$ can reach $20 \, \text{km s}^{-1}$. Note that the final residual made on each fit (which, from equation 14, must be noise only) is a perfect Gaussian distribution with a standard deviation of $0.5 \, \text{km s}^{-1}$. We conclude that, as long as the optics are not changed, the DIR remains stable and the real calibration map of a target observed in a direction different from the zenith only depends on the instrumental parameters p of the geometrical model $M(x, y, p)$. Note that a standard deviation of $0.5 \, \text{km s}^{-1}$ on the fit of the calibration laser map does not mean that our precision on the wavelength calibration will be the same. This result better gives a lower limit on the calibration precision. The wavelength calibration of the actual data is discussed in the next section.
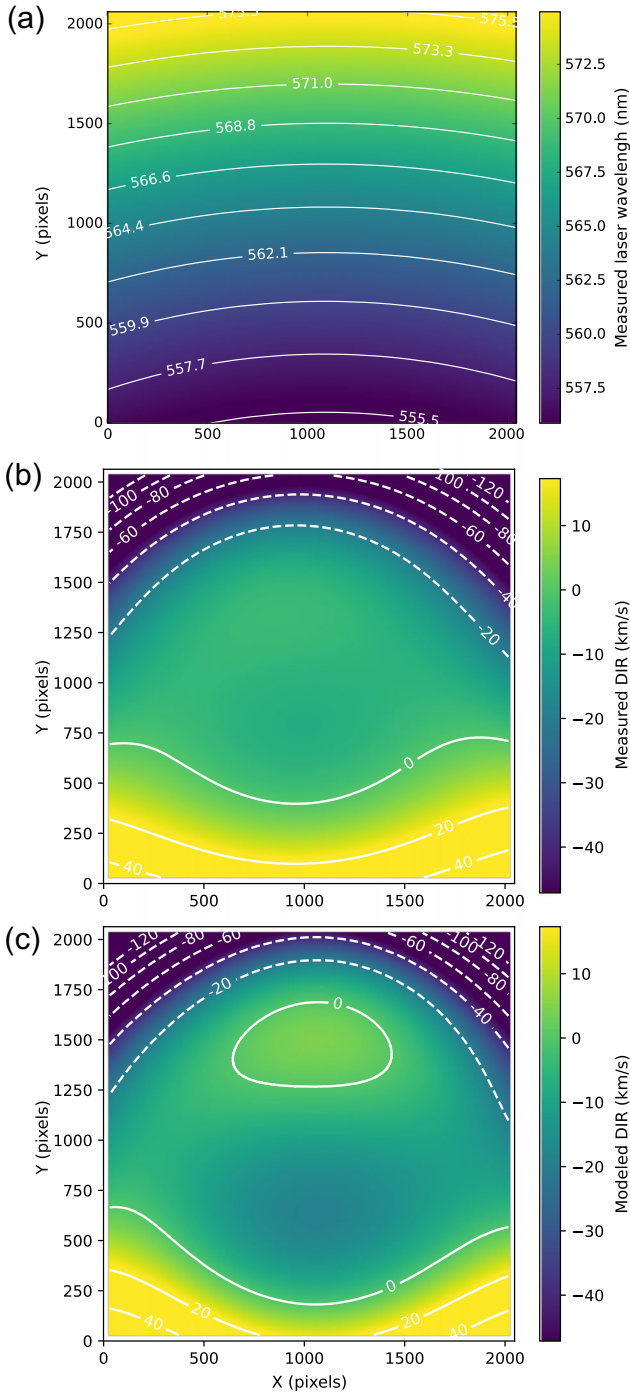
Figure 3. (a) Calibration laser map. The real wavelength of the calibration laser is 543.5 nm. The measured wavelength depends on the incident angle θ of the incoming light with respect to the interferometer axis (see Fig. 1). (b) Distortion Induced Residual once the structural model is subtracted. The wavelength error is given in terms of velocity error at H α. (c) Modelled DIR computed with the astrometric distortion model. Contours are solid when the value is positive and dashed when negative.

2.2.3 Fit of the sky velocity

We have measured the velocity of the sky lines over the whole FOV by extracting 1600 spectra at each point of a 40×40 grid. Each sky spectrum was integrated over a 30×30 pixels box to improve its signal-to-noise ratio. But, as explained in Section 2.2.1 the high
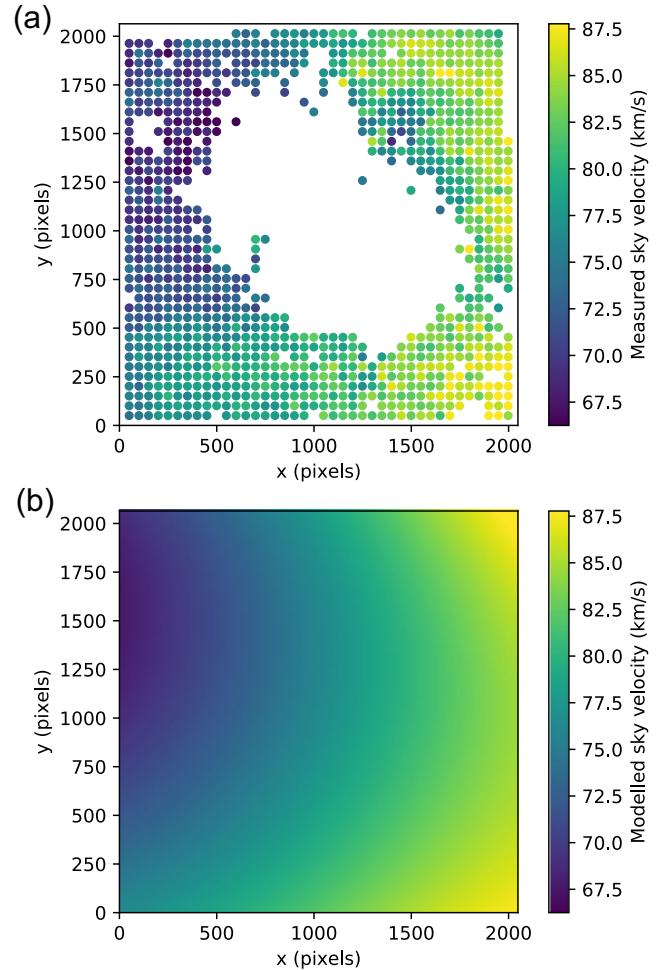
Figure 4. (a) Measured velocity of the sky lines in the SN3 filter on integrated spectra of 30×30 pixels in SITELLE's FOV. The points where no sky lines could be measured and the points having an uncertainty greater than 1.7 km s^{-1} are not displayed (and were not used for the fit). The white area (depopulated from reliable measurements) corresponds to the central region, where the continuum flux is very high. The main goal of the fitted model shown below is to give an estimate of the sky velocity in this area. (b) Velocity model of the sky lines computed from the calibration laser map model and fitted over the velocity points shown in (a). Fitted parameters of the model are reported in Table 2 and residuals of the fit are shown in Fig. 5.

level of continuum near the centre of the galaxy prevents any precise measure over a large part around the centre of the field (see Fig. 4). We have thus used the model described in the previous section to compute the real instrumental parameters during the observation of M 31 by fitting our model to the measured velocity of the sky lines (Table 2). Note that the rotation angle has been fixed at 0 because there is a strong degeneracy between the rotation angle and φ_c which leads to unphysical values of the structural parameters without giving an appreciable difference in the precision of the fit.

With this method, we have been able to estimate the sky lines velocity in the central region of the FOV where no sky lines could be measured and reduce the initial velocity gradient of more than 15 km s^{-1} (Fig. 4) down to a much flatter error with a standard deviation of 2.21 km s^{-1} (Fig. 5). This is considered to be our systematic uncertainty and has been added to all the estimations of the uncertainty on the velocity measurements.

Table 2. Fitted parameters of the calibration laser map model for the wavelength calibration of M 31 based on the measured sky lines velocity. The reference camera is Cam1.

Beamsplitter-detector distance (d)	23.8 cm
X angle from the optical axis to the centre(λ_c)	−0°.47
Y angle from the optical axis to the centre(φ_c)	15°.44
Tip-tilt angle of the detector along X (α)	0°.25
Tip-tilt angle of the detector along Y (β)	−0°.43
Rotation angle of the detector (γ)	0° (fixed)
Calibration laser wavelength	543.37 nm

(a)

(b)
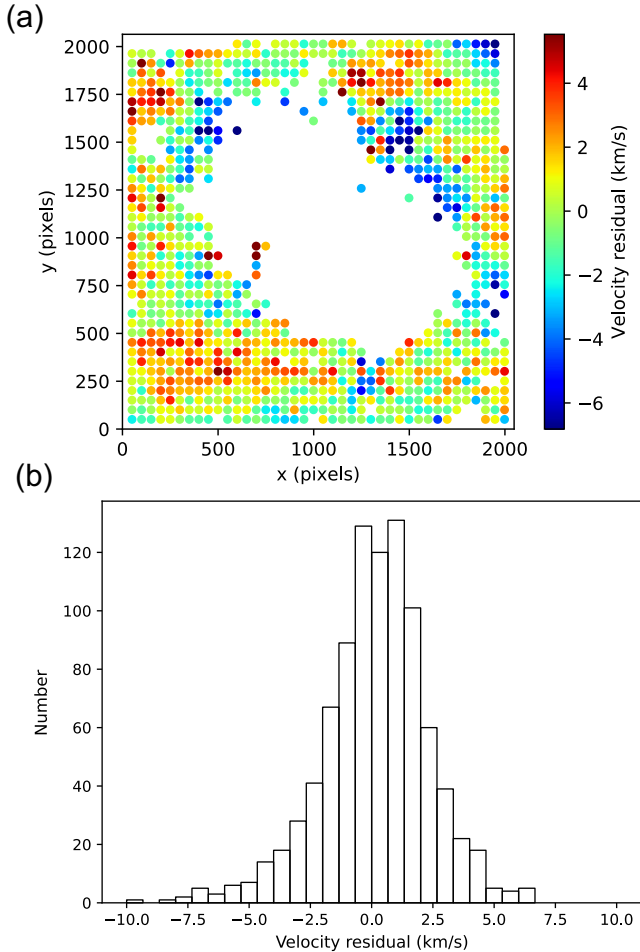
Figure 5. (a) Map of the residual error on the velocity calibration after the computed model is removed. (b) Histogram of the residual error on the velocity calibration corresponding to the map presented above. The median of the distribution is 0.25 km s^{-1} and its standard deviation is 2.21 km s^{-1}. This systematic uncertainty has been added to all velocity measurements.

Nevertheless, we must admit that the standard deviation is still higher than the 0.5 km s^{-1} obtained with the direct fit of the calibration laser map (see Section 2.2.2). We see two possibilities regarding the accuracy of the DIR. First, the stability of the DIR, which is not recomputed (only the instrumental parameters can be fitted), is ensured as long as the optics are not touched. Sadly, no calibration laser cube has been taken during the night of the observation, which was the first night of the run. The next night, one of the two cameras (Cam1) was removed to perform some tests and was put back in place but with a rotation of 0°.8 (this rotation corresponds to the angle θ in the model described in Section 2.2.2),

making the measurement of the DIR from the calibration laser, obtained after the changes on Cam1, much less precise. We have tried to simulate the real calibration laser map (and thus the real DIR) at the date when M 31 was observed by rotating Cam1 on the calibration data obtained a few days after with no real success. That is why, even if this possibility cannot be discarded, we do not believe that the difference we see is due to the camera change. The other possibility comes from the fact that our model has only been tested with green laser cubes (543.5 nm) and it is possible that the DIR calculated at 543.5 nm may not be exactly the same in the SN3 filter (i.e. around 660 nm). If we consider that a deviation of 1 pixel in the distortion pattern can account for up to 6 km s^{-1}, small variations of the refractive index of the beamsplitter could explain why the error is structured and has a higher than expected standard deviation (Fig. 5).

### 2.3 Astrometric calibration

The astrometric calibration model can be divided into three levels of refinement. The first level starts with the determination of five general registration parameters: the target coordinates in the image, its celestial coordinates and the angle between the image's *Y*-axis and the north. This rough model is arguably more precise near the centre of the frame, where the effects of the optical distortions are minimal. Indeed, the second level includes a distortion model based on the Simple Image Polynomial (SIP) convention (Hook, Simple & Polynomial 2008). All the parameters estimated for the first and the second levels of astrometric calibration can be written into any FITS header (Hanisch et al. 2001) and interpreted with most FITS viewers (e.g. SAO Image DS9[2]). But, even with an SIP distortion model, the calibration error can be as large as 1.5 arcsec in the corners of the image (Figs 6 and 7). The third level of refinement relies on two distortion maps (one for each axis of the image) which are computed from the residual between the SIP calibration model and the real position of the stars in the image; an error on the calibration smaller than 0.3 arcsec (1 image pixel) is then reached. While the first level only requires a few stars to get an acceptable calibration, the other two require the observation of a densely populated star field to precisely determine the distortion model.

2.3.1 First level: general registration parameters

The coordinates at the centre of the FOV are generally known with an uncertainty smaller than 15arcsec and the rotation angle cannot vary by more than 5°. Many optical modifications between each run since SITELLE's commissioning explain this large uncertainty on the rotation angle from one observation to another; these are expected to be much less numerous from now on. Nevertheless, a good and robust estimate of the general parameters is obtained with a two-step registration process.

(i) A first reduction of the uncertainty is made from the correlation of the 2D histogram of the real list of positions of all the stars visible in the image and the positions of the stars found in a catalogue. In the case of M 31, we have used the *Gaia* DR1 catalogue(Gaia Collaboration 2016a,b). With this method, the two lists do not need to contain exactly the same stars. The peak of the correlation image will provide the shift between both lists with an uncertainty that depends on the size of the 2D histogram bins
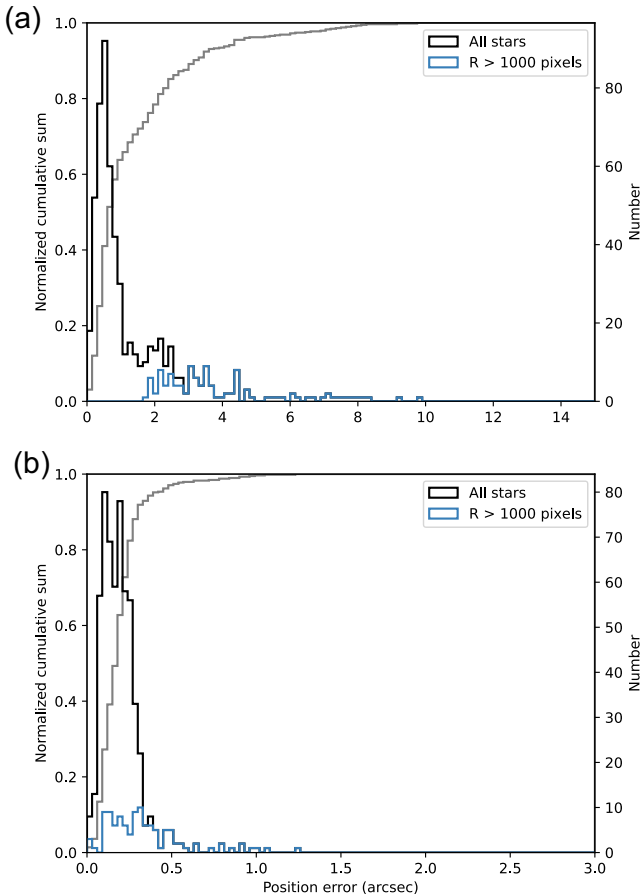
[2] http://ds9.si.edu/site/Home.html

Figure 7. Position error in one region of the FOV of M 31 taken far from the centre where the distortions are the most important. The crosses indicate the computed position of the stars after the first calibration step, in red, the second calibration step, in orange, and the third calibration step, in green.

region is small, we have used an image of a field in NGC 6960, obtained on the same night, to compute the SIP parameters.

2.3.3 Third level: residual distortion maps

Even if the SIP model performs remarkably well at describing the distortions of the FOV, the error can be as large as 1.5 arcsec, especially in the corners of the field where distortions are the strongest (Fig. 6). Primarily because of SITELLE's optics whose aberrations are radially dependant and secondarily because of the image quality that is severely degraded in the corners for reasons still unknown. To reduce this error down to less than 1 pixel, we have no choice but to compute two distortion maps, one for each axis (shown in Fig. 8). The interpolation of the displacement along both axes between the stars is modelled with Zernike polynomials which are well suited to model wavefront distortions.

The resulting calibration must have a precision better than 1 pixel (0.32 arcsec), everywhere in the field. It seems difficult to compare with other catalogues since the catalogue we use (*Gaia* DR1) is, by far, the one which contains the more stars with the highest precision. A comparison of our catalogue of emission-line point-like sources (see Section 3) with another catalogue is made in Section 3.4. It suggests an upper-limit uncertainty of 0.21 arcsec on our calibration that supports our calibration.

2.4 Flux calibration

The flux calibration was performed from two calibration sources: (1) the spectrum of the spectrophotometric standard star GD71 (Bohlin 2003), obtained in 2016 January, which is used to eliminate as much as possible any strong wavelength dependence; (2) the median combination of a set of 10 images of the standard star HZ 4 (Bohlin, Dickinson & Calzetti 2001) obtained right after the end of the cube observation with photometric conditions similar to the observation conditions. The exact value of the interferometer's

Figure 6. (a) Histogram of the position error after the first calibration level. The median of the error is around 2 arcsec and can be as large as 14 arcsec in the corners of the image. (b) Histogram of the position error after the second calibration level. The median of the error is now smaller than 0.3 arcsec which is more than six times better than the first level median error. The histograms of the stars in the corners, defined as having a radius with respect to the centre of the field greater than 1000 pixels, i.e. 5.35 arcmin, are shown in blue. The cumulative histograms are shown in light grey.

(generally of the order of 10 pixels, i.e. 3 arcsec). Note that a brute force search, which consists in a systematic search along a range of possible angles, must first be used to find the rotation angle that maximizes the amplitude of the histogram peak.

(ii) A brute force method, which consists in a systematic search through all the possible sets of parameters – each parameter, being explored over a given range of possible values, is used to find the set of parameters which maximizes the total flux measured in the image at the positions projected from the catalogue. When a maximum of stars are present at those positions, the total flux is at its highest.

2.3.2 Second level: SIP distortion model

Once the general registration parameters are known, it is possible to match the position projected from a catalogue with the stars on the image, especially near the centre where the error is less than a few pixels. The parameters of a fourth-order SIP distortion model are found with a least-squares Levenberg–Marquardt minimization algorithm (Levenberg 1944; Marquardt 1963) to reduce as much as possible the distance between both lists (which now must contain the same stars). As the number of suitable stars in M 31's central
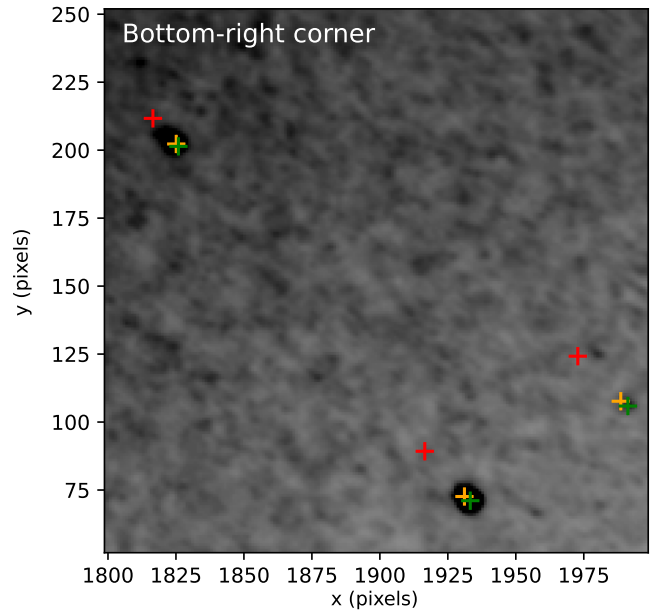
Figure 8. Residual distortion maps along the *Y* (*a*) and *X* (*b*) axes used for the third level of astrometric calibration. The position error is given in pixels. 1 pixel has a dimension of 0.32 arcsec.

Figure 9. Positions of the *HST* fields over SITELLE's FOV used to refine the flux calibration.
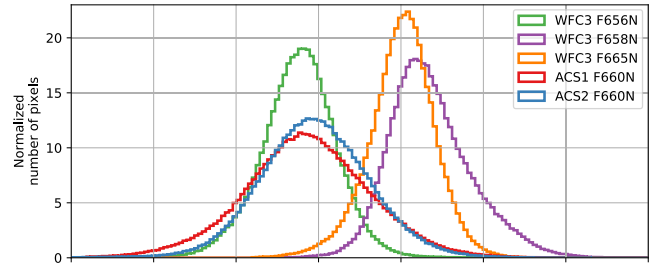
Figure 10. Histograms of the flux ratio between the integrated frames (which simulate *HST* frames) and the real *HST* frames. The median and standard deviation of theses distributions are reported in Table 3.

Table 3. Median and standard deviation of the histograms of the flux ratios shown in Fig. 10. λ_{mean} is the pivot wavelength of the *HST* filters.

Instrument	Filter	λ_{mean} (in nm)	Field	Median [Std] (in per cent)
WFC3 UVIS1	*F656N*	656.15	WFC3	93.8 [2.3]
WFC3 UVIS1	*F658N*	658.56	WFC3	101.5 [2.6]
WFC3 UVIS1	*F665N*	665.60	WFC3	100.1 [2.1]
ACS WFC	*F660N*	659.95	ACS1	94.3 [4.0]
ACS WFC	*F660N*	659.95	ACS2	94.7 [4.1]

modulation efficiency (ME), which acts essentially as an additional throughput loss, is the major source of uncertainty on the absolute flux calibration (Martin & Drissen 2016). Interferometric images of the laser source have been obtained before and after the observation of the target in order to measure the variation of ME at the calibration laser wavelength (543.5 nm) with respect to its nominal value (85 per cent). We have measured a loss of 11.7 per cent. The initial flux calibration of M 31 in the SN3 filter has been corrected for this loss (thus multiplied by a factor 1.13). But given the possible uncertainty on this estimate, we have double-checked it using *Hubble Space Telescope* (*HST*) narrow-band images of the target. The advantage of *HST*'s narrow-band filters is that they can easily be simulated by integrating the spectral cube over the filter's well-known transmission curve. As SITELLE's cube flux is expressed in erg cm^{-2} s^{-1} Å^{-1} and given the filter transmission curve $F(\sigma)$, the integrated flux $\tilde{\phi}_{\mathrm{F}}$, expressed in erg cm^{-2} s^{-1} Å^{-1}, is

$$\tilde{\phi}_{\mathrm{F}} = \frac{\int_{-\infty}^{+\infty} \phi(\sigma) F(\sigma) \mathrm{d}\sigma}{\int_{-\infty}^{+\infty} F(\sigma) \mathrm{d}\sigma}. \tag{15}$$

If one converts the flux in terms of surface brightness, expressed in erg cm^{-2} s^{-1} Å^{-1} per *HST* pixel surface ($S_{\mathrm{HSTCamera}}$), i.e.

$$\tilde{B}_{\mathrm{F}} = \frac{\tilde{\phi}_{F}}{S_{\mathrm{SITELLE}}} S_{\mathrm{HSTCamera}}, \tag{16}$$

with $S_{\mathrm{SITELLE}} = 0.32^2$ arcsec^2, the image $\tilde{B}_{\mathrm{F}}$, once properly aligned, can be directly compared with the *HST* frame. We have made this comparison for three different regions of the FOV (called WFC3, ACS1 and ACS2, shown in Fig. 9) and four different filters (*F656N*, *F658N*, *F665N* and *F660N*). Histograms of the flux ratio between the integrated frames and the *HST* frames are presented in Fig. 10 and the first moments of their distributions are listed in Table 3.
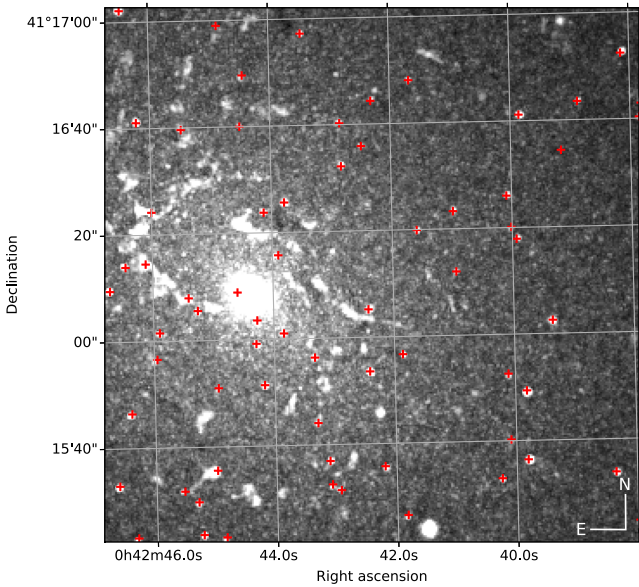
Figure 11. Cropped region of the detection frame around the centre of M 31. Red crosses indicate the positions of the sources of the catalogue.

2.4.1 Relative flux calibration

We can estimate the pixel-to-pixel relative uncertainty from the flux ratio maps. But we must be careful with the absolute calibration of the Hubble images. Indeed, the average sky background intensity reported in the WFC3 Instrument Handbook is $3.8 \times 10^{-18} \, \text{erg} \, \text{cm}^{-2} \, \text{s}^{-1} \, \text{Å}^{-1} \, \text{arcsec}^{-2}$ at 6000 Å that must be compared to the surface brightness of M 31 which ranges in our FOV from 5×10^{-17} to $5 \times 10^{-15} \, \text{erg} \, \text{cm}^{-2} \, \text{s}^{-1} \, \text{Å}^{-1} \, \text{arcsec}^{-2}$ accounting for 1.4 per cent in the WFC3 field and around 7 per cent in the ACS fields. Also, from the WFC3 Instrument Handbook the quoted photometry accuracy is around 2–3 per cent. This uncertainty alone is sufficient to explain the difference in the median ratio in the different fields especially the 7 per cent difference between the $F656N$ filter and the $F658N$ and $F665N$ filters obtained in the same region at the centre of the field. It is thus difficult to assert that there is no gradient in the absolute flux calibration smaller than 8 per cent. In the ACS fields, a higher limit of 4 per cent on the relative calibration can be deduced from the standard deviation of the ratio histograms. In the central region, the smaller standard deviation is around 2 per cent which sets the higher limit on the relative flux calibration in this region.

2.4.2 Absolute flux calibration

To get the most conservative estimate on the absolute flux calibration correction we have computed the mean of the five median values of the flux ratios (considered with their uncertainty) to obtain a mean flux ratio of 96.9 ± 1.4 per cent which has been used to correct the flux calibration of our data.

3 EMISSION-LINE SOURCES NEAR THE CENTRE OF M 31

While the main objective of the SN3 data cube was to study the diffuse gas around M 31's nucleus, we were delighted to see a very large number of point-like sources appearing as we scanned the reduced cube. Since the brightest of them could likely be used to
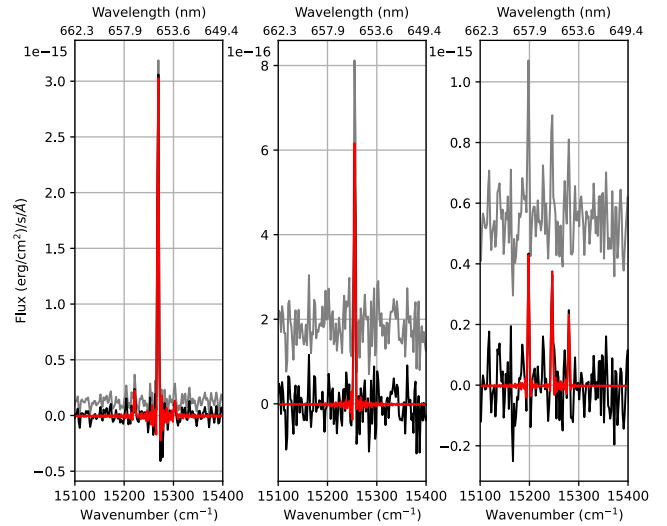
Figure 12. Examples of extracted spectra. The raw spectrum is in grey, the background-corrected spectrum is in black and the fit is in red. Only the region around the H α line is shown.

assess the validity of our calibrations, we put some efforts into the systematic detection and characterization of point-like emission-line sources in this cube. The following section thus describes the detection technique, the catalogue resulting from this analysis and comparisons with previous catalogues, as well as a discussion of some interesting sources.

3.1 Source detection

The relatively large velocity range ($\sim 800 \, \text{km} \, \text{s}^{-1}$) due to galactic rotation near the centre of M 31 requires a dedicated algorithm to detect emission-line sources. We devised such an algorithm, which aims at detecting an excess of flux in at least one spectral channel for a given pixel with respect to its surroundings. First, the spectrum of this pixel is replaced by the median spectrum of the 3×3 pixels box centred on it (matching the mean seeing during the observations). The median spectrum of a 9×9 pixels box (excluding the central 3×3 pixels) is then subtracted. The maximum flux of this background-subtracted spectrum is then stored in a detection map at the location of the pixel under investigation (see Fig. 11). This map, which therefore provides the level of emission of each pixel above its surrounding background, highlights numerous point sources, the brightest foreground stars and some very bright portions of the filaments of diffuse gas around the core of the galaxy. Finally, we have checked this detection map by eye for the presence of point-like sources which spectra have been extracted and fitted manually.

3.2 Extraction and fit of the sources

Once the identification of candidates was completed, the background-subtracted spectrum of each candidate has been integrated in a 3×3 pixels box around the central pixel. This time, the background spectrum was chosen to be the median spectrum of a 30×30 pixels box (excluding the central 3×3 box), which was found to be the optimal setting to maximize the signal to noise in the whole galaxy though it might not be optimal near the very centre of M 31 where there is an important background gradient.

Table 4. Results of the detection of our sources in the LGGS ratio frames when they are considered together and independently (see the text for details). Detection is said non-applicable (N/A) when the source is situated in the saturated region near the centre of M 31 (in at least one of the frame when frames are considered together). A source is considered undetected in both frames if it is not detected in any of the frames and if it is not situated in a saturated region. A source is considered detected in both frames when it is detected in at least one of the frames.

LGGS ratio frame	detected	undetected	N/A
H α/R	533	147	117
[O III]/B	389	376	32
H α/R or [O III]/B	595	117	85

so the flux must be corrected for this aperture loss. We have simulated our integration model on a synthetic star with a Moffat PSF (Moffat 1969). The real centre of the synthetic star was randomly positioned, with a uniform distribution, in the central pixel to mimic the fact that the 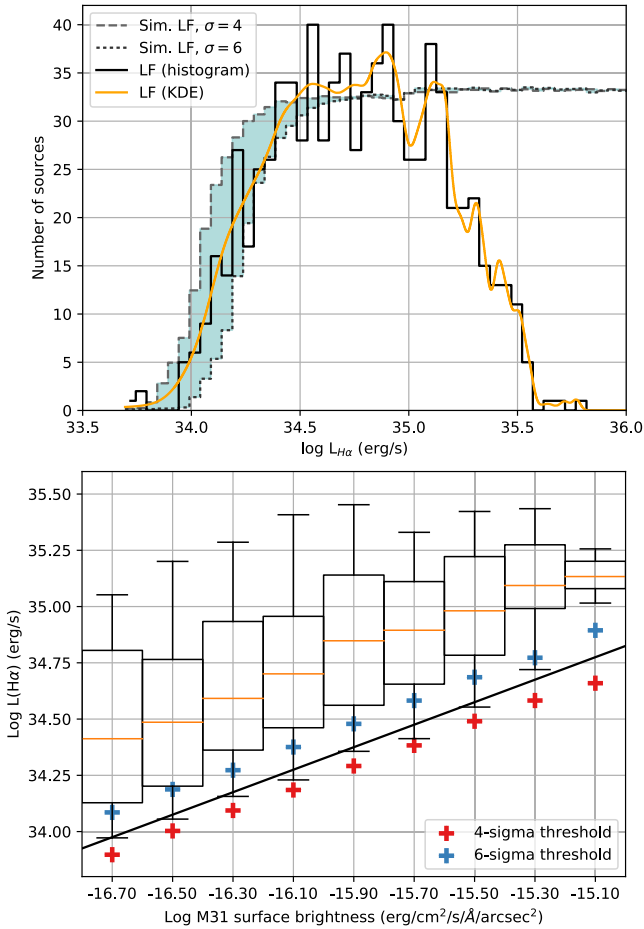real centre of the integrated source can be anywhere in the central pixel of the 3×3 box. The shape parameters of the synthetic star (width and the Moffat parameter β) were taken from a fit of multiple stars in the deep frame of the cube (the deep frame represents the integral of the cube along the spectral axis). From the analysis of 100 000 trials, we can conclude that the measured flux must be multiplied by 1.88 ± 0.07.

The final correction made on the measured flux is the product of the ME loss, the flux calibration obtained from the comparison with Hubble images and the computed PSF loss which gives a final correction factor FC:

$$FC = 1.13 \times \frac{1}{0.969 \pm 0.014} \times 1.88 \pm 0.07 = 2.199 \pm 0.088.$$

(17)

The systematic relative uncertainty made on the measured flux, independently of the uncertainty due to the SNR of the fitted spectra, is thus 4 per cent.

3.3 Description of the catalogue

We have detected and catalogued a total of 797 H α emitting sources in our FOV (see Table B1). The radial velocity and the broadening of the lines as well as the flux of H α, [N II] λ6584, and the combined flux of [S II] λ6717 and [S II] λ6731 have been reported in the catalogue with their corresponding uncertainty. When the SNR of a line was smaller than 5 and thus not clearly detected, we have reported an estimation of the upper limit of the flux. This upper limit was considered to be the minimum value between the estimated amplitude plus three times its uncertainty or five times the uncertainty. As the lines are modelled with the same velocity, the [S II] and [N II] lines are always present in the fit results but the amplitude uncertainty might be much higher than its measured value (as already mentioned, a line was considered detected for an SNR higher than 5). In this case, the uncertainty used to calculate the upper limit on the [S II] or the [N II] flux is strongly related to the background noise.

Examples of spectra are shown in Fig. 12. The reported SNR is the maximum intensity attained by the spectrum (i.e. by the H α or [N II] λ6584 line) corrected for the background and the median intensity and divided by the standard deviation of the residual of the fit (see Section 3.2).

Figure 13. *Top:* H α luminosity function $L_{H\alpha}$ of the catalogued sources, uncorrected for extinction. The kernel density estimation (Rosenblatt 1956; Parzen 1962) of the luminosity function is also plotted as an orange line. The histograms simulated for a detection threshold at 4σ and 6σ are shown. The blue region between both simulated histograms indicates where the luminosity function should fall for a detection threshold between 4σ and 6σ. *Bottom:* simulated 90 per cent completeness (luminosity under which the completeness is smaller than 90 per cent) with respect to the background flux for a detection threshold at 4σ and 6σ. The function from equation (19) is drawn in solid black. The box and whiskers plot represents the distribution of the luminosity of the catalogued sources per bins of the underlying galaxy's surface brightness. Whiskers are set at the 5th and 95th percentiles of the distributions.

The spectrum was then fitted with a model made of five emission lines (H α, [N II] λ6548, [N II] λ6584, [S II] λ6717, [S II] λ6731) plus a flat background. Note that the He I λ6678 line was not detected anywhere. The analytic model describing the line spread function of the emission lines is the convolution of a sinc, the instrumental line shape, and a Gaussian, an approximation of the real line shape (see Fig. 12). The line model, described in detail in Martin et al. (2016), has three varying parameters: amplitude, velocity and broadening of the Gaussian; the FWHM of the sinc line is known and fixed as it depends only on the maximum OPD of the interferogram (see equation 5 of Martin et al. 2016). All the five emission lines were considered to share the same velocity and the same broadening.

We have chosen to integrate the source spectrum into a 3×3 box in order to maximize the signal-to-noise ratio of our spectrum. But the point spread function (PSF) clearly extends beyond this limit,

Figure 14. Spectra, cropped around the Hα lines and the [N II] doublet, of the seven sources having an SNR greater or equal to 7 and undetected in the LGGS ratio images (see the text for details). The fit of the three lines is shown in solid red. The source id, as well as the width of the Hα line are indicated above each spectrum. At the bottom right, we show the histogram of the line broadening of all the sources (black line) and the broadening of the seven displayed sources (orange bars). Two of the three objects with a broadening larger than 100 km s^{-1} have a split profile (see Section 3.3.3). The apparent bimodality of the histogram (with two peaks at 22 and 0 km s^{-1}) is an artefact of the fitting algorithm which can be reproduced when fitting low-signal-to-noise ratio lines (see the text for details).

We have cross-matched our sources with the catalogues of Halliday et al. (2006) and Merrett et al. (2006), aimed at the detection and characterization of planetary nebulae specifically targeting the [O III] λ5007 line, and reported the corresponding ID in Table B1. We have detected 304 of the 332 sources detected in [O III] by Merrett et al. (2006, a 91.5 per cent completeness) and 149 of the 154 sources observed by Halliday et al. (2006, a 96.8 per cent completeness). A comparison of our measured velocity with the velocity reported by Halliday et al. (2006) is made in Section 3.4.

Supernovae remnants and novae were detected but have been removed from the catalogue, the first ones because they are not point-like and the second ones because of their transient nature. They are discussed independently in Section 3.6.

3.3.1 Luminosity function and completeness

The luminosity function, uncorrected for extinction, of the sources in the catalogue is shown in Fig. 13 and has been calculated with the relation

$$L_{H\alpha} = 4\pi D^2 F(H\alpha), \tag{18}$$

D being the distance to the centre of M 31 assumed to be 0.783 Mpc (Mochejska et al. 1999). Note that from Azimlu et al. (2011) and Walterbos & Braun (1992), maximum luminosity of planetary nebulae is $\sim 5\,10^{35}$ erg s^{-1}, which is the case of 99.6 per cent of our sources. Our detectability limit in terms of flux $F(H\alpha)$ is around 10^{-16} erg s^{-1} with 4.1 h of integration over the very bright background

Figure 15. Spectra of sources showing split profile. The observed spectrum is displayed in black. We can clearly see the departure from the fitted model, in red. The measured broadening of the lines is reported in parenthesis. The top spectrum is clearly an expanding shell. The redshifted and the blueshifted com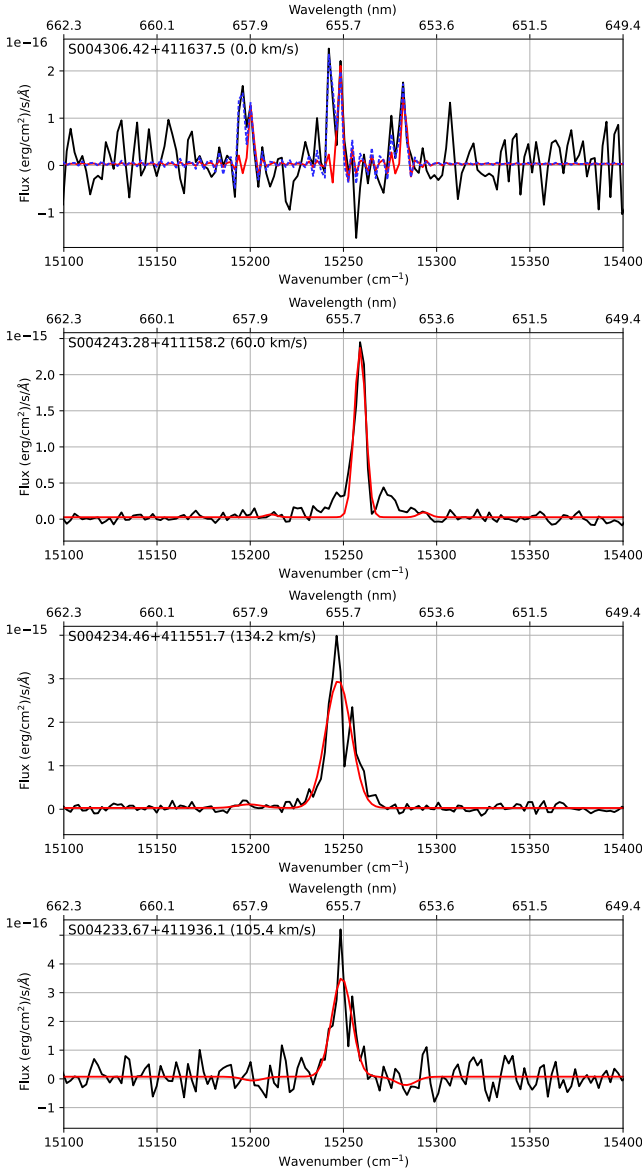ponents have been fitted together. The resulting fit is plotted in dotted blue. The measured expansion velocity is $90.7 \pm 1.4\,\mathrm{km\,s^{-1}}$. As it was fitted with a sinc model, the broadening of the lines is, by definition, $0\,\mathrm{km\,s^{-1}}$.

of M 31 which is certainly one of the worst case scenario for a Fourier transform spectrometer.

We have verified the completeness of our sample by simulating the detection of 10 million randomly positioned emission-line point sources in one channel of a spectral cube. Considering only the photon noise contribution, the noise is the same in every channel and its amplitude is the square root of the total number of counts accumulated in each pixel (Drissen et al. 2012, 2014; Maillard et al. 2013). Starting with a map of the total number of counts in each pixel, we can add a group of randomly positioned sources with a log-uniform flux distribution and compute its square root to obtain a map of the photon noise. Each source has its flux concentrated in only 1 pixel and one channel which greatly simplify the simulation

Figure 16. *Top:* velocity measured with SITELLE versus velocity measured by Ha06. The one-to-one line is shown in dotted grey. *Bottom:* histogram of the velocity difference with Ha06. The median of the distribution is shown in orange.

of the detection process. The noise is multiplied by $\sqrt{9}$ to simulate the 3×3 binning used for the detection and the extraction of the spectra. The flux of the 1 pixel star is divided by 1.88 to simulate the loss of flux in the wings of the PSF. It is also divided by 1.25 to simulate the fact that its real flux is distributed as a sinc line spread function with a width of 1.25 channels.[3] All the pixels showing a value above the background level plus a given number of times the calculated noise σ are considered as detected sources. Note that the 10 million sources were simulated by sets of a thousand sources in a SITELLE frame of 4 million pixels. So that the probability of having multiple sources at the same pixel is negligible. The histograms of the detected sources for a threshold at 4σ and 6σ are shown in Fig. 13. They reproduce well the slope of the luminosity function at low-luminosity level, confirming that the completeness is good at a detection threshold of $\sim 5\sigma$.

In terms of homogeneity of the completeness in the FOV, it is clear that the level of detectability changes with the surface brightness of M 31. We have used the results of the simulation detailed above to compute the 90 per cent completeness (i.e. the limit luminosity under which the completeness falls under 90 per cent) with respect

---

[3] We recall that the flux F of a sinc line of amplitude A and width W is $F = AW$.
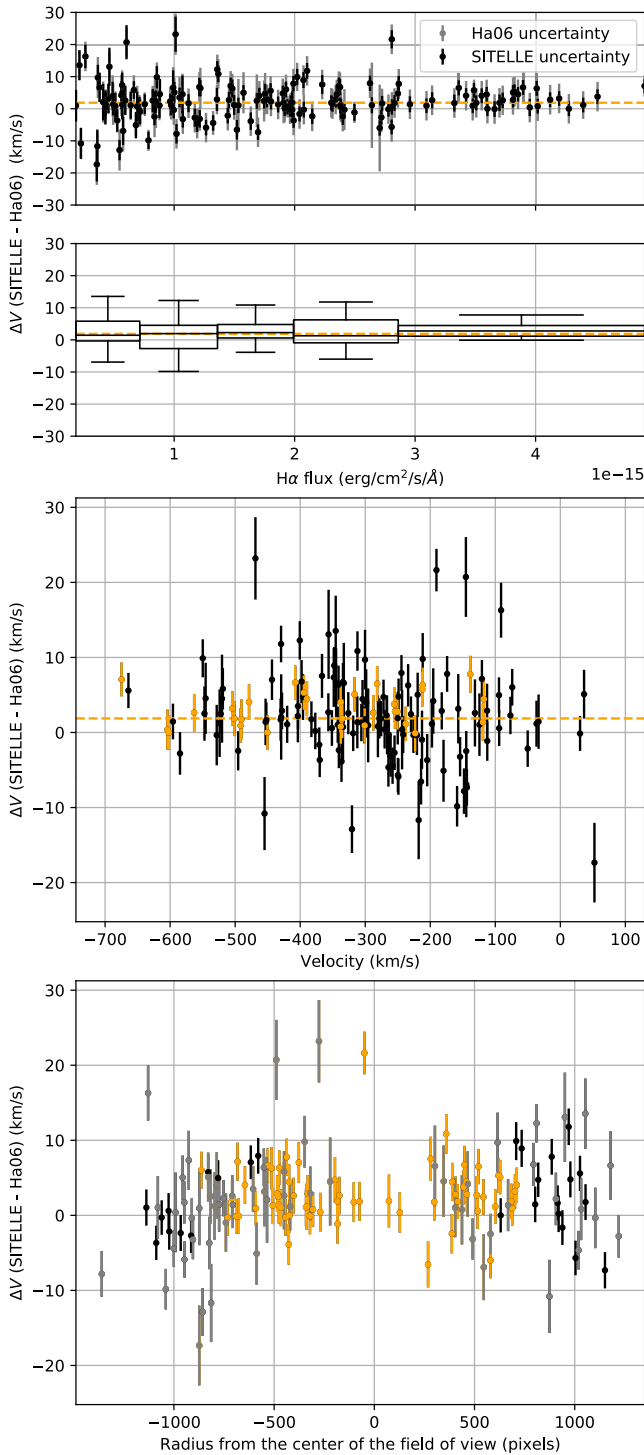
Figure 17. *Top:* velocity difference with Ha06 versus H α flux. The box plot represents the distribution of the difference by bins of equal number of data points. *Centre:* velocity difference with Ha06 versus velocity. The 10 per cent most luminous sources are shown in orange *Bottom:* velocity difference with Ha06 versus radius with respect to the centre of the FOV (the radius is set negative when the distance along the declination axis, i.e. the *y*-axis, is negative). The sources in orange are situated in the region where the sky lines velocity could not be measured. Their calibration thus heavily relies on the model described in Section 2.2.1.
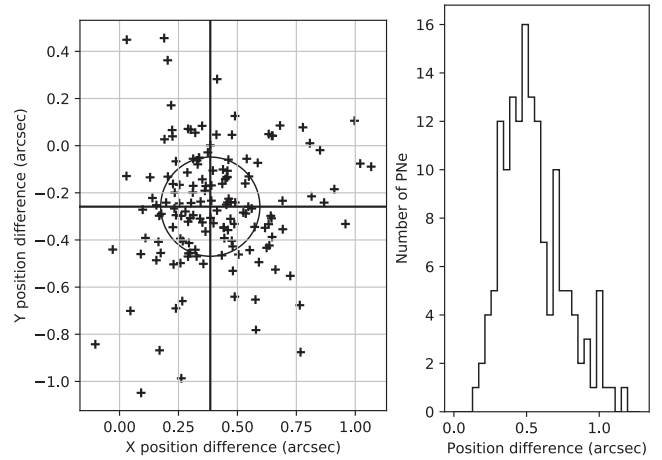
Figure 18. *Left:* scatter of the position differences along the *X* and *Y* axes of the image of the sources compared with Ha06. The vertical and the horizontal black lines indicate the median of the differences in *X* and *Y*, respectively. A circle represents the standard deviation. *Right:* histogram of the position differences with Ha06.
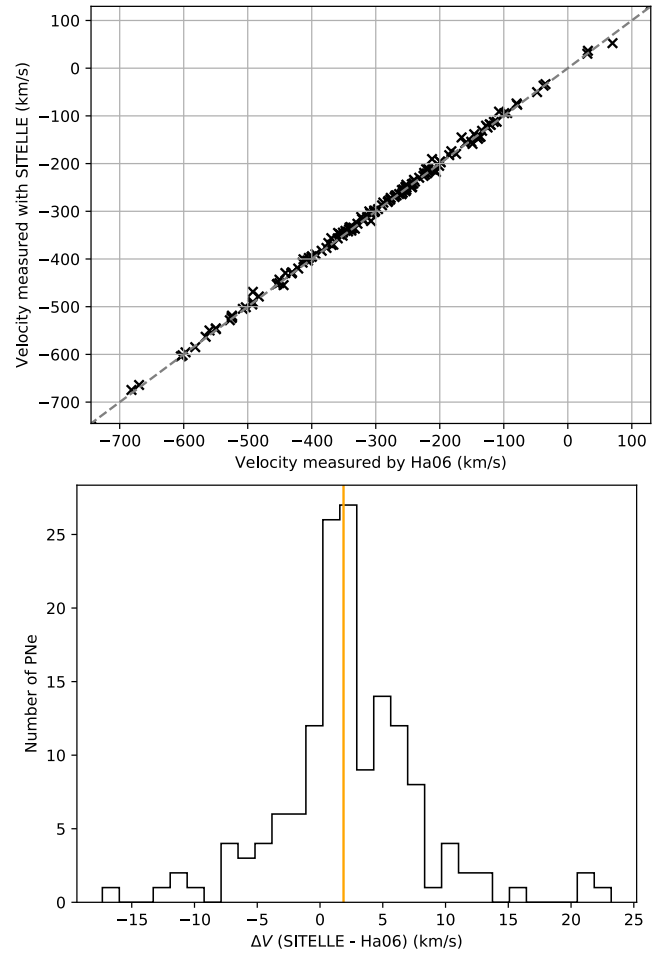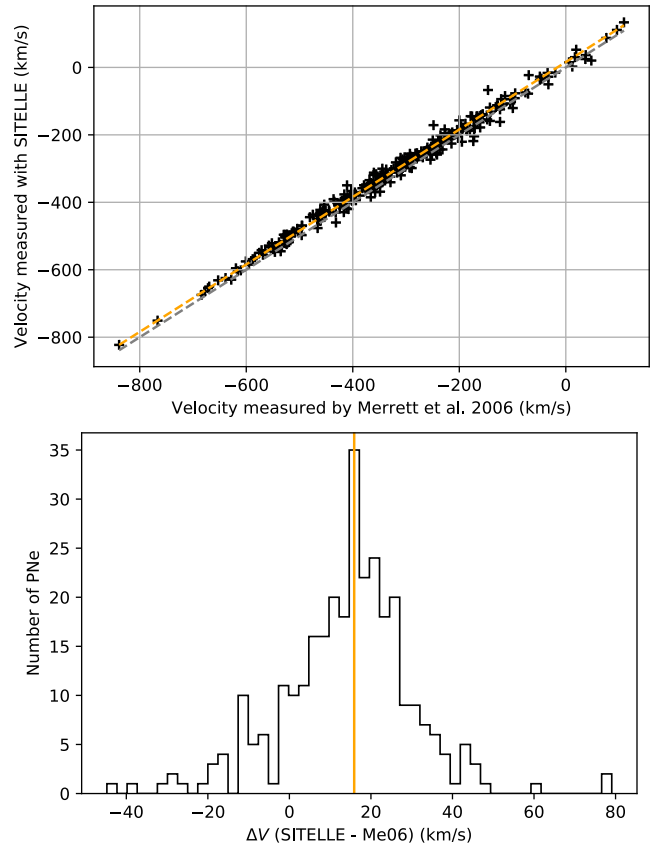

Figure 19. *Top:* velocity measured with SITELLE versus velocity measured by Me06. The one-to-one line is shown in dotted grey. The same line corrected for the median of the distribution of the velocity difference (see bottom histogram) is shown in dotted orange. *Bottom:* histogram of the velocity difference with Me06. The median of the distribution is shown in orange.
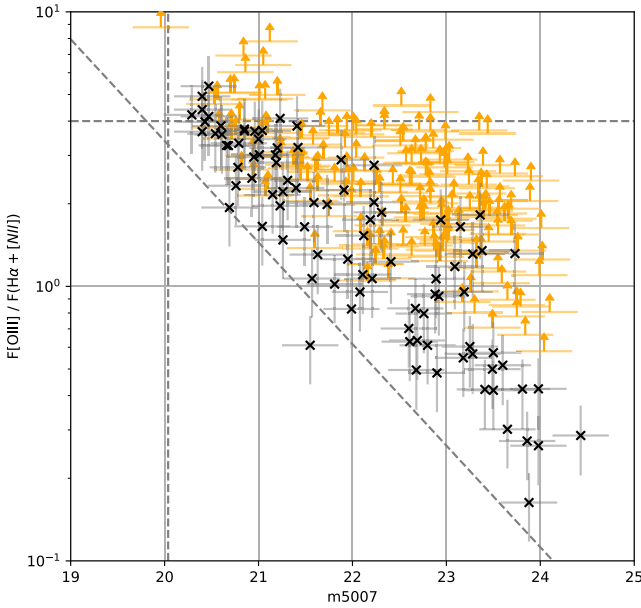
Figure 20. Flux ratio $F([O\,III])/F(H\,\alpha + [N\,II])$ with respect to the relative m_{5007} magnitude from Me06. The sources which [N II] line flux could only be given an upper limit are plotted in orange. The other are plotted with black crosses. The error bars are also shown. The region in this graph where all the planetary nebulae are supposed to be is defined by the three dotted grey lines. The vertical line corresponds to the planetary nebulae luminosity function zero-point quoted by Ciardullo et al. (2002) and the two others are defined in Herrmann et al. (2008).

to M 31's surface brightness B for a detection threshold of 4σ and 6σ (see Fig. 13). The function that best fits the mean of the simulated data is

$$\log(L_{H\alpha}) = 0.5\log(B) + 42.325. \tag{19}$$

We have also reported in Fig. 13, a box and whisker plot representing the distribution of the luminosity of the catalogued sources per bins of the underlying galaxy's surface brightness. Whiskers are set at the 5th and 95th percentiles of the distributions. If we examine closely the whiskers corresponding to the 5th percentile of the luminosity distribution we can see that they nearly all fall between the 4σ and 6σ simulations, except for the highest brightness bin that contains much less sources than the others. This result confirms the adopted simulation process.

3.3.2 LGGS cross-match

We have verified if our sources were also detectable in the images of the Local Group Galaxies Survey (LGGS; Massey et al. 2006; field F5). To do so, we have divided the narrow-band images centred on $H\alpha$ and $[O\,III]\lambda5007$ by their corresponding broad-band images R and B and checked by eye if a source could be seen at the location of our emission-line sources. Note that a region of 2.5 arcmin and 15 arcsec at the centre of M 31 in, respectively, the R and B images is saturated and cannot be studied; sources in this region are marked with 'N/A' in the corresponding columns. We report in Table 4 the number of detected and undetected sources in each ratio image. A total of 595 of our sources were detected in at least one of the LGGS ratio images while 117 were clearly not detected; 85 are not detected in one of the frame but are situated in a saturated region in the other frame, in which case the non-detection is less clear. If, in most cases, those undetected sources have a relatively low SNR (which may explain the non-detection), with a median of 5, seven

of them have an SNR larger than 7 and should have shown up in the LGGS ratio images. It indicates that they could display new or variable emission lines (the field F5 of the LGGS data has been obtained on 2001 September 22). Another interesting fact is that all those objects share a similar spectral morphology, namely that they display a broad $H\alpha$ emission line (broader than the instrumental resolution) with no sign of [N II] (see Fig. 14). From the histogram shown in Fig. 14, it appears that this broadening is significantly larger than that of the vast majority of the catalogued sources.

The histogram of Fig. 14 shows an apparent bimodality (with two peaks at 22 and $0\,\text{km s}^{-1}$) which is an artefact of the fitting algorithm that can be reproduced when fitting low-signal-to-noise ratio lines. The bimodality being clearly separated at $4\,\text{km s}^{-1}$ (with no values of the broadening at $4\,\text{km s}^{-1}$), all the measured broadening values smaller than $4\,\text{km s}^{-1}$ have been removed from the catalogue.

3.3.3 Split profiles

Four sources are displaying split profiles which are shown in Fig. 15. They have been added the commentary 'Split' in the catalogue. The first object (S004306.42+411637.5) is clearly an expanding nebula with a velocity difference of $90.7\pm1.4\,\text{km s}^{-1}$ between the two components. The second object (S004243.28+411158.2) could also be seen as a single line with two satellites lines or a broadened line with some absorption (like a PCygni profile). No [S II] lines are detected in its spectrum, and no stellar source is seen in the deep SN3 image. The three others show a broad, split $H\alpha$ line, with no evidence for forbidden lines. A relatively bright point source is visible in the deep SN3 image in all cases.

3.3.4 Elongated PSF

A non-negligible fraction of the outer portion of the FOV shows an elongated PSF. The origin of the elongation is still unknown and could be related to an error in the model of the telescope or the optics of SITELLE (Drissen et al., in preparation). The 89 sources found in the affected region were marked with the commentary 'elongated PSF'. As 90 per cent of the flux is concentrated in the principal lobe of the PSF, the effect on the completeness is likely to be under 10–15 per cent. The computed flux is also likely to be underestimated by the same amount. The measured velocity suffers the same bias as the sky lines and has thus been calibrated. No velocity bias should be observed.

3.4 Comparison with the catalogue of Halliday et al. (2006)

Halliday et al. (2006, henceforth Ha06) have measured the radial velocity of 723 planetary nebulae in M 31, 154 of which are present in the field observed with SITELLE. We have detected 148 of them (96 per cent) which is an excellent completeness rate considering the fact that our detection is based on the $H\alpha$ while theirs is based on the usually brighter [O III] line.

We have plotted their velocities against ours and found that they fall very near the one-to-one line (Fig. 16). The histogram of the velocity difference with Ha06 is also shown in Fig. 16. The median difference is $1.8\,\text{km s}^{-1}$ and the standard deviation is $6.1\,\text{km s}^{-1}$. If we quadratically sum the uncertainty reported by Ha06 and ours, the median uncertainty on the velocity difference is $5.6\,\text{km s}^{-1}$. These results confirm at the same time their calibration and ours as long as both quoted uncertainties are correct. Because we could not have any precise measurement of the OH lines velocity in the centre of the FOV, we have been using a model to estimate the velocity

Table 5. Novae visible in our data. The associated spectra are shown in Fig. 21.

ID	Detection date	Atel #	Type	Coordinates	Reference
M31N 2016-03b	2016 February 26.737 UT	#8785	–	0:42:19.54 +41:11:14.0	Hornoch & Kucakova (2016)
M31N 2016-03c	2016 February 7.753 UT	#8787	–	0:42:49.25 +41:16:40.16	Hornoch, Kucakova & Wolf (2016)
M31N 2016-03d	2016 March 17.768 UT	#8838	–	0:43:01.58 +41:14:08.7	Hornoch & Vrastil (2016)
M31N 2016-05b	2016 May 28.046 UT	#9098	Fe II	0:42:42.88 +41:15:27.1	Darnley & Williams (2016)
M31N 2016-08d	2016 August 17.102 UT	#9388	Fe II	0:42:23.53 +41:17:19.8	Williams et al. (2016)

Table 6. Characteristics of the observed supernova remnants.

ID	other ID	Coordinates	Radial velocity (km s^{-1})	Broadening (km s^{-1})
SNR1	1050[a]	0:42:50.50 +41:15:56.19	−320.5 ± 3.0	58.4 ± 2.1
SNR2	–	0:42:25.07 +41:17:34.79	−429.5 ± 4.9	59.2 ± 4.6
SNR3	#41[b], r2-57[c]	0:42:24.68 +41:17:30.79	−101.0 ± 3.8	47.2 ± 3.1
SNR4	#43[b]	0:42:25.67 +41:17:49.19	−351.5 ± 3.7	37.3 ± 3.3

Notes. [a]Stiele et al. (2011) and Sasaki et al. (2012).
[b]Lee & Lee (2014).
[c]Williams et al. (2004).

correction in the centre based on the values obtained on the borders of field (see Section 2.2 and Fig. 4). Any error on the model would translate into a correlation between the velocity difference and the radius with respect to the centre of the image. This is not the case (see Fig. 17). We have also checked that there was no correlation with the velocity and that the difference was getting smaller at higher flux (Fig. 17). Note that Ha06 are measuring the [O III] lines while we are providing the flux in H α; those two properties are only partially correlated.

When comparing the position of our sources with the position reported by Ha06, we find a median difference of 0.46 arcsec (Ha06 quote an absolute uncertainty of 1 arcsec, with a relative uncertainty of 0.4 arcsec on their positions), with a standard deviation of 0.21 arcsec, which is smaller than one SITELLE pixel and very similar to our estimate of the uncertainty (see Fig. 18).

The comparison with the catalogue of Ha06 therefore confirms the quality of our wavelength and astrometric calibration.

3.5 Comparison with the catalogue of Merrett et al. (2006)

Merrett et al. (2006, henceforth Me06) have measured the radial velocity of 2615 planetary nebulae in M 31, 330 of which are present in the field observed with SITELLE. We have detected 305 of them (92 per cent) which is a good completeness rate considering the fact that our detection is based on the H α while theirs is based on the usually brighter [O III] line. The quoted uncertainty on their measurement is 17 km s^{-1} with a systematic error around 5–10 km s^{-1} which is much higher than the uncertainty of Ha06's catalogue. The distribution of the velocity difference with their catalogue is shown in Fig. 19. This 'distribution' standard deviation of 16 km s^{-1} is strongly dominated by the uncertainty of their measurement and confirms their estimation. The distribution is also biased by 16 km s^{-1} which is also consistent with the comparison they made with the data of Ha06 (they found a systematic difference of 17 km s^{-1}).

We can further check the quality of our photometry by comparing the flux ratio $F([O III])/F(H \alpha + [N II])$ with respect to the relative m_{5007} magnitude reported in their catalogue. Note that the [O III] flux also comes from their value of m_{5007} since Me06:

$$m_{5007} = -2.5 \log (F([O III])) - 13.74 . \tag{20}$$

We can see that most of our common sources fall in the wedge-like zone where we can find all the planetary nebulae of the Local Group Galaxies M31 and M33 (Schönberner et al. 2010). This zone is located between the lines defined by Herrmann et al. (2008):

$$\log \left(\frac{F([O III])}{F(H \alpha + [N II])} \right) = -0.37 M([O III]) - 1.16 \tag{21}$$

and

$$\log \left(\frac{F([O III])}{F(H \alpha + [N II])} \right) \simeq 4, \tag{22}$$

where $M([O III])$ is the absolute magnitude in the [O III]λ5007 line which has been computed from the relation

$$M([O III]) = m_{5007} - A_V - \mu, \tag{23}$$

considering the values of the reddening $E(B - V) = 0.062$ mag (Schlegel, Finkbeiner & Davis 1997) and a distance D to M 31 of 750 kpc (Freedman et al. 2000) which translate to an interstellar extinction $A_V = 3.1 E(B - V) = 0.19$ mag and a distance modulus $\mu = 5 \log (D) - 5 = 24.38$ mag. We have chosen here the same references as Ciardullo et al. (2002) to keep its value of the planetary nebulae luminosity function zero-point $M_\star = -4.53$ mag which is also reported in Fig. 20.

3.6 Objects not listed in the catalogue

3.6.1 Novae

Between 65 and 100 novae erupt each year in M31 (Darnley et al. 2006; Chen et al. 2016; Soraisam et al. 2016), about a third of which are detected. Between January 11 (first nova detected in 2016) and August 24 (the day of our observations), seven nova candidates were detected in SITELLE's FOV,[4] but only two of them (Nova M31 2016-08d and 05b) have been spectroscopically confirmed, both as type Fe II novae. Spectra of five of our sources displayed an excessive broadening compared to all other objects (see the lower right panel of Fig. 14): all of them were indeed in the list of nova candidates. These objects are listed in Table 5 but not in the catalogue because of their transient nature; their spectra are shown in
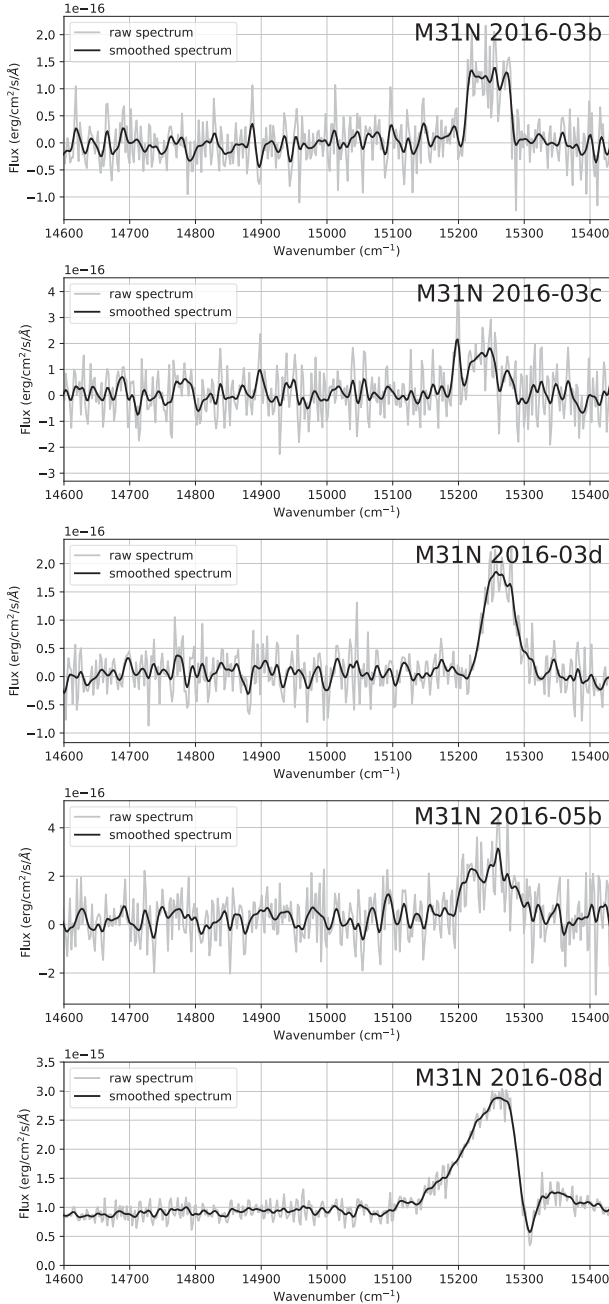
---

[4] http://www.rochesterastronomy.org/sn2016/novae.html

Figure 21. Novae spectra extracted from the data cube. Note that the integration region is smaller than the object size to enhance the SNR. The real flux of the nova should be considered as a lower limit and may be up to 50 per cent higher. The background-subtracted spectrum is plotted in grey and the fit is plotted in black.

Fig. 21. We therefore confirm the nova nature of three previously unconfirmed candidates (2016-03b, 03c and 03d), whereas two candidates (2016-06b and 03e) do not display obvious nova signature in our data.

3.6.2 Supernova remnants

Three supernova remnants (SNRs) were previously known in SITELLE's field (Williams et al. 2004; Sasaki et al. 2012; Lee & Lee 2014). These SNRs are all presumably from type Ia events since there is no signature of recent star formation in our FOV:
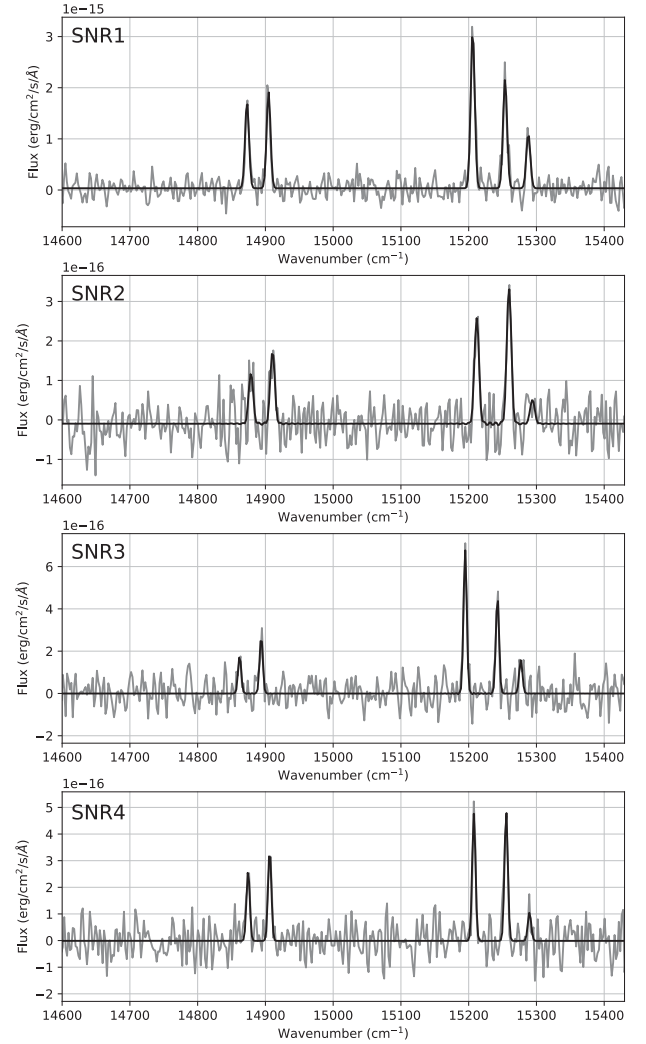

Figure 22. Integrated spectra of the supernovae remnants. The spectrum of the SNR3 has not been integrated over the whole visible region but only on its brightest knot. The background-subtracted spectrum is plotted in grey and the fit is plotted in black.

recent studies found no H II regions (Azimlu et al. 2011) or young clusters (<1 Gyr; Kang et al. 2011) and the dust seems to be only heated by the old stellar population (Viaene et al. 2014).

They clearly stand out in our cube, and we have detected one more (labelled SNR2). We have used the same criteria as Lee & Lee (2014), based on Braun & Walterbos (1993), to classify this SNR: a [S II]/H α ratio greater than 0.4 (0.464 ± 0.086 in our case) and the absence of a blue star. The basic characteristics of these four SNRs are presented in Table 6. The corresponding spectra are shown in Fig. 22.

SNR1: SNR1 is clearly present in the H α and [S II] images (field 5) provided by the Local Group Survey (Massey et al. 2006) and it is classified as an SNR by Sasaki et al. (2012) but it has not been selected as an SNR candidate by the team, although our spectrum clearly shows strong [S II] lines; all its lines are broader than the instrumental resolution. A detailed analysis of this object, #1050 in the catalogue of Stiele et al. (2011), in the X-ray and optical wavelengths can be found in Sasaki et al. (2012). They report an H α flux of $7.5\,10^{-15} \pm 4.4\,10^{-16}$ erg cm^{-2} s^{-1} and a mean [S II] flux of $7.7\,10^{-15} \pm 1.5\,10^{-15}$ erg cm^{-2} s^{-1} which compares well with our fluxes of $6.8\,10^{-15} \pm 4.7\,10^{-16}$ erg cm^{-2} s^{-1} for H α
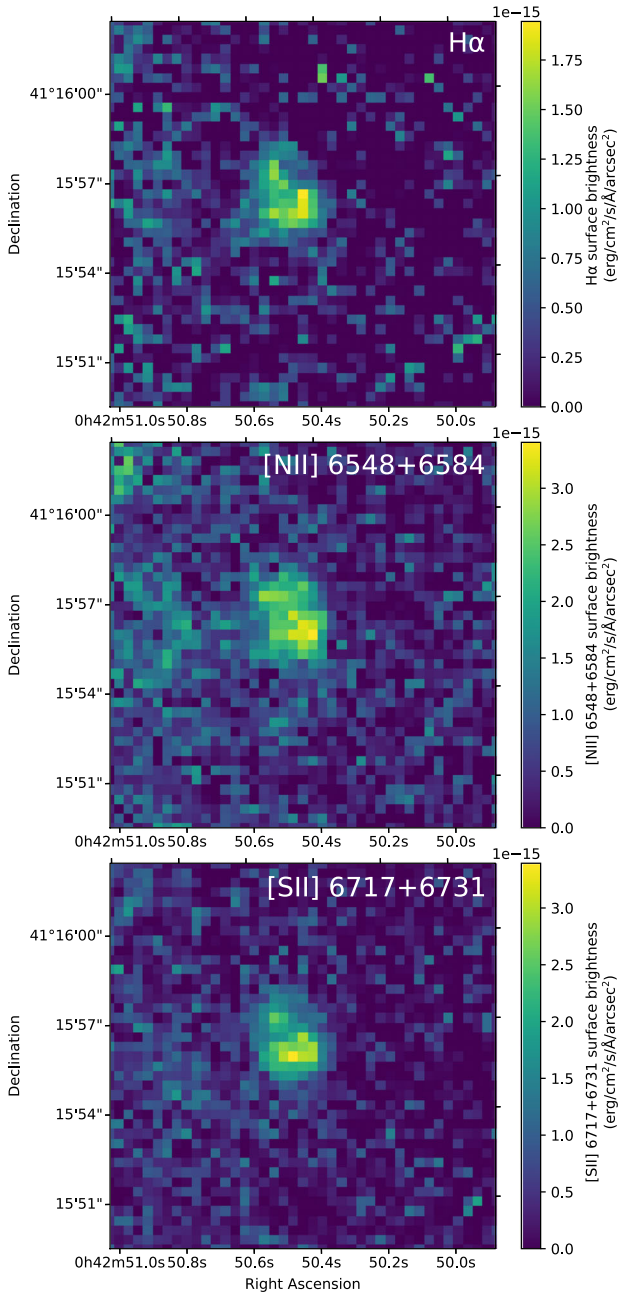
Figure 23. Flux maps in H α, [N II] and [S II] of the supernova remnant SNR1. It is catalogued as the X-ray source 1050 in Stiele et al. (2011). It has been classified as an SNR and studied in detail by Sasaki et al. (2012).

and $5.8\,10^{-15} \pm 3.2\,10^{-16}$ erg cm^{-2} s^{-1} for [S II] measured on the integrated spectrum shown in Fig. 22. Images of its spatially resolved emission in H α, [N II] and [S II] are shown in Fig. 23.

SNR2, SNR3 and SNR4: Three of the four SNRs in SITELLE's field (Lee & Lee 41 and 43, as well as our new SNR2) are within 30 arcsec of each other (see Fig. 24). If SNR3 shows a velocity much different from SNR2 and SNR4, the latter have a velocity difference of only 80 km s^{-1} (see Table 6), suggesting that they could be related to the same event making the remnant 60 pc wide which is a little larger than the galactic SNR NGC 6960. The detection map, which shows the highest intensity in the spectrum of each pixel relatively to its neighbourhood is shown in Fig. 24. A detailed study of the SNR3 (named r2-57 in their article) in the X-ray, optical and radio wavelengths can be found in Williams et al. (2004). In their Fig. 3,
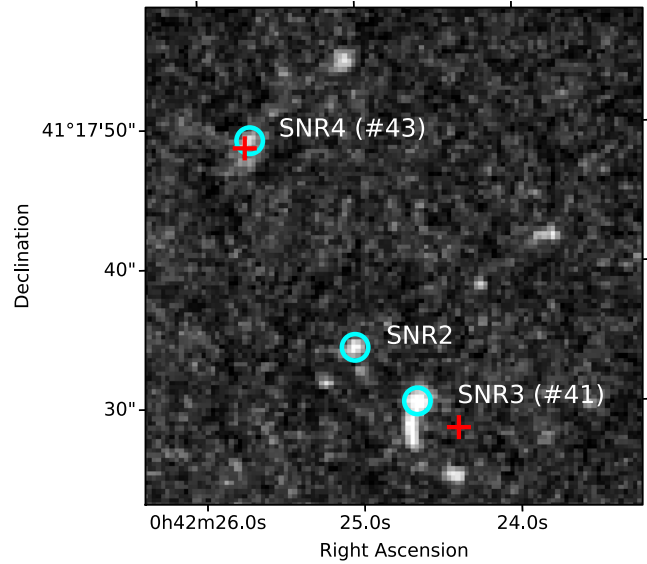

Figure 24. Small part of the detection map (see Section 3.1) showing the proximity of three of the four supernovae remnants detected in the central region of M 31. Red crosses show the position of the centre of the remnants reported in the catalogue of Lee & Lee (2014). Blue circles indicate the regions integrated to compute the spectra shown in Fig. 22. Note that we have chosen the brightest node of the remnant which has no reason to be the same as the central position reported by Lee & Lee (2014).

the [S II] emission of the SNR2 can also be seen but nothing's found in the [O III] image of the LGGS (Massey et al. 2006) while the SNR3 is clearly visible. The H α surface brightness map of SNR2 and the [N II] surface brightness map of SNR4 (Lee & Lee 43), the most extended of all four SNRs in our field (8 arcsec $\sim$ 30 pc), are shown in Fig. 25.

4 CONCLUSIONS

We have documented and demonstrated the quality of a set of general calibration methods for SITELLE that has been applied to a spectral cube covering the centre of M 31 in the H α–[N II]–[S II] range (649–684 nm). Although the main target of this data set was to study line ratios and kinematics of the diffuse gas surrounding the core of M 31 (Melchior et al., in preparation), one of the first side effects of this project is the publication of the larger and the most precise catalogue of the H α-emitting point sources in the central region where the background flux is so high that emission-line sources are less detectable than on the outskirt. This is also a very interesting test since the detection of these sources has been made in the worst possible conditions for a Fourier transform spectrometer considering the very high continuum background of the target. Nevertheless, the number of known emission-line point sources in this region is more than two times larger than the previously published catalogues, five novae spectra have been obtained as long as spatially resolved data of four supernovae remnants, one of them being a new discovery. Great care was taken to compare the obtained data with the best catalogues (Halliday et al. 2006; Merrett et al. 2006) and images (Massey et al. 2006) of this region which demonstrate the quality of the calibration as long as the completeness of the catalogue. A deeper analysis of this catalogue combined with the data obtained in the [O III]–H β range will be made in the subsequent articles. We believe that the quality of the calibration made will prove useful for all the other studies made with this data cube.
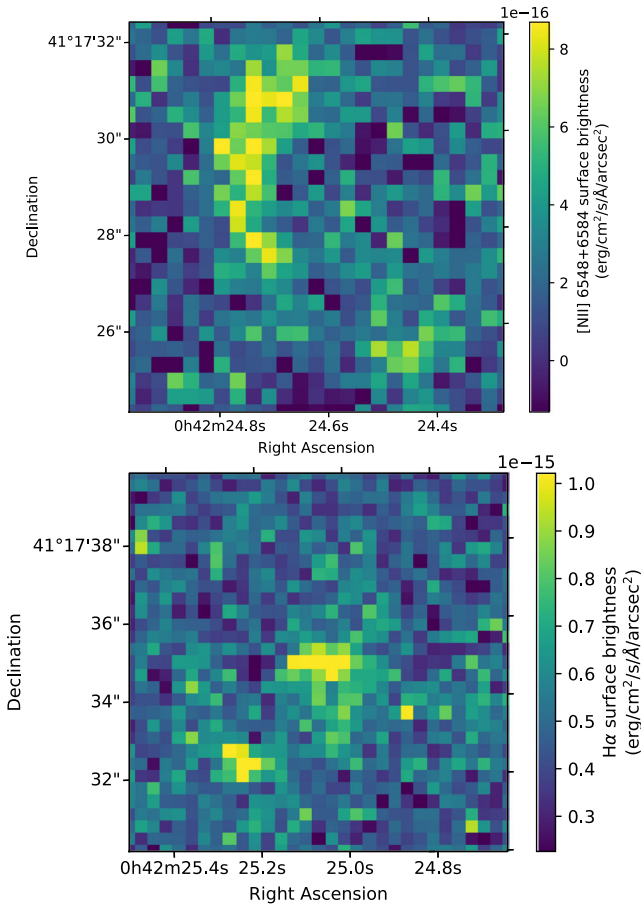
Figure 25. *Top:* [N II] surface brightness map of the supernova remnant SNR3 (#41 of Lee & Lee 2014, r2-57 in Williams et al. 2004). *Bottom:* H α surface brightness map of the newly discovered supernova remnant SNR2.

ACKNOWLEDGEMENTS

REFERENCES

Azimlu M., Marciniak R., Barmby P., 2011, AJ, 142, 139
Baril M. R. et al., 2016, in Evans C. J., Simard L., Takami H., eds, Proc. SPIE Conf. Ser. Vol. 9908, International Society for Optics and Photonics. SPIE, Bellingham, p. 990829
Bohlin R. C., 2003, in Arribas S., Koekemoer A., Whitmore B., eds, The 2002 HST Calibration Workshop: Hubble after the Installation of the ACS and the NICMOS Cooling System. STScI, Baltimore, MD, p. 115
Bohlin R. C., Dickinson M. E., Calzetti D., 2001, AJ, 122, 2118
Braun R., Walterbos R. A. M., 1993, A&AS, 98, 327
Chen H.-L., Woods T. E., Yungelson L. R., Gilfanov M., Han Z., 2016, MNRAS, 458, 2916
Ciardullo R., Feldmeier J. J., Jacoby G. H., de Naray R. K., Laychak M. B., Durrell P. R., 2002, ApJ, 577, 31
Darnley M. J., Williams S. C., 2016, Astron Telegram, 9143
Darnley M. J. et al., 2006, MNRAS, 369, 257
Davis S. P., Abrams M. C., Brault J. W. J. W., 2001, Fourier Transform Spectrometry. Academic Press, New York
Drissen L., Bernier A.-P., Rousseau-Nepton L., Alarie A., Robert C., Joncas G., Thibault S., Grandmont F., 2010, in McLean I. S., Ramsay S. K., Takami H., eds, Proc. SPIE Conf. Ser. Vol. 7735, International Society for Optics and Photonics. SPIE, Bellingham, p. 77350B
Drissen L. et al., 2012, in McLean ed., Proc. SPIE Conf. Ser. Vol. 8446, Ground-based and Airborne Instrumentation for Astronomy IV. SPIE, Bellingham, p. 84463S
Drissen L., Rousseau-Nepton L., Lavoie S., Robert C., Martin T., Martin P., Mandar J., Grandmont F., 2014, Adv. Astron., 2014, 1
Freedman W. L. et al., 2000, ApJ, 553, 47
Gaia Collaboration G., 2016a, 595, A1
Gaia Collaboration G., 2016b, A&A, 595, A2
Grandmont F., 2006, PhD thesis, Université Laval
Grandmont F., Drissen L., Mandar J., Thibault S., Baril M. R., 2012, in McLean I. S., Ramsay S. K., Takami H., eds, Proc. SPIE Conf. Ser. Vol. 8446, Ground-based and Airborne Instrumentation for Astronomy IV. SPIE, Bellingham, p. 84460U
Halliday C. et al., 2006, MNRAS, 369, 97
Hanisch R. J., Farris A., Greisen E. W., Pence W. D., Schlesinger B. M., Teuben P. J., Thompson R. W., Warnock A., 2001, A&A, 376, 359
Herrmann K. A., Ciardullo R., Feldmeier J. J., Vinciguerra M., 2008, ApJ, 683, 630
Hook R. N., Simple T., Polynomial I., 2008, in Shopbell P., Britton M., Ebert R., eds, ASP Conf. Ser. Vol. 347, Astronomical Data Analysis Software and Systems XIV. Astron. Soc. Pac., San Francisco, p. 491
Hornoch K., Kucakova H., 2016, Astron. Telegram, 8785
Hornoch K., Vrastil J., 2016, Astron. Telegram, 8838
Hornoch K., Kucakova H., Wolf M., 2016, Astron. Telegram, 8787
Kang Y., Rey S.-C., Bianchi L., Lee K., Kim Y., Sohn S. T., 2011, ApJS, 199, 37
Lee J. H., Lee M. G., 2014, ApJ, 786, 130
Levenberg K., 1944, Q. Appl. Math., 2, 164
Maillard J. P., Drissen L., Grandmont F., Thibault S., 2013, Exp. Astron., 35, 527
Marquardt D. W., 1963, J. Soc. Ind. Appl. Math., 11, 431
Martin T., 2015, Phd thesis, Université Laval
Martin T., Drissen L., 2016, in Reylé C., Richard J., Cambrésy L., Deleuil M., Pécontal E., Tresse L., Vauglin I., eds, Proc. Annu. Meeting French Soc. Astron. Astrophys. Lyon, SF2A-2016. p. 23
Martin T., Drissen L., Joncas G., 2012, in Radziwill N. M., Chiozzi G., eds, Proc. SPIE Conf. Ser. Vol. 2, Software and Cyberinfrastructure for Astronomy II. SPIE, Bellingham, p. 84513K
Martin T., Drissen L., Joncas G., 2015, in Taylor A. R., Rosolowsky E., eds, ASP Conf. Ser. Vol. 495, Astronomical Data Analysis Software and Systems XXIV (ADASS XXIV). Astron. Soc. Pac., San Francisco, p. 495
Martin T. B., Prunet S., Drissen L., 2016, MNRAS, 463, 4223
Massey P., Olsen K. A. G., Hodge P. W., Strong S. B., Jacoby G. H., Schlingman W., Smith R. C., 2006, AJ, 131, 2478
Merrett H. R. et al., 2006, MNRAS, 369, 120

Mochejska B. J., Macri L. M., Sasselov D. D., Stanek K. Z., 1999, AJ, 120, 810

Moffat A. F. J., 1969, A&A, 3, 455

Parzen E., 1962, Ann. Math. Stat., 33, 1065

Rosenblatt M., 1956, Ann. Math. Stat., 27, 832

Sasaki M., Pietsch W., Haberl F., Hatzidimitriou D., Stiele H., Williams B., Kong A., Kolb U., 2012, A&A, 544, A144

Schlegel D. J., Finkbeiner D. P., Davis M., 1997, ApJ, 500, 525

Schönberner D., Jacob R., Sandin C., Steffen M., 2010, A&A, 523, A86

Shara M. M., Drissen L., Martin T., Alarie A., Stephenson F. R., 2016, MNRAS, 465, 739

Soraisam M. D., Gilfanov M., Wolf W. M., Bildsten L., 2016, MNRAS, 455, 668

Stiele H., Pietsch W., Haberl F., Hatzidimitriou D., Barnard R., Williams B. F., Kong A. K. H., Kolb U., 2011, A&A, 534, A55

Viaene S. et al., 2014, A&A, 567, A71

Vincenty T., 1975, Surv. Rev., 23, 88

Walterbos R. A. M., Braun R., 1992, A&AS, 92, 625

Williams B. F., Sjouwerman L. O., Kong A. K. H., Gelfand J. D., Garcia M. R., Murray S. S., 2004, ApJ, 615, 720

Williams S. C., Darnley M. J., Thorstensen J. R., Klusmeyer J. A., Shafter A. W., Henze M., Hornoch K., Chinetti K., 2016, Astron. Telegram, 9411

APPENDIX A: RELATION BETWEEN THE INCIDENT ANGLE AND THE MEASURED WAVENUMBER

When light enters a Michelson interferometer at a null incident angle (see Fig. A1), the OPD x is simply two times the mechanical distance Δx between the actual position of the moving mirror and the position where both mirrors are at the same distance of the beamsplitter (known as the zero path difference position, ZPD):

$$x = 2\Delta x. \tag{A1}$$

When the incident angle θ is different from 0, the OPD is known to be (see e.g. Davis, Abrams & Brault 2001)
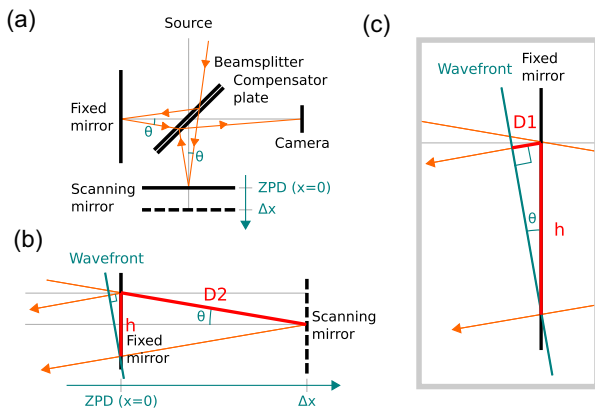
$$OPD = x \cos(\theta). \tag{A2}$$

Figure A1. (a) Optical path of the light at an incident angle θ in a classical Michelson interferometer. (b) Superposition of the optical path followed by the light in the fixed mirror arm and the moving mirror arm. The moving mirror is at a mechanical distance Δx from the ZPD (the position where both mirrors are at the same distance of the beamsplitter). $D2$ is the optical distance crossed by light along the moving mirror path. (c) Zoomed-in portion of figure (b) showing the optical distance $D1$ crossed by light along the fixed mirror path.
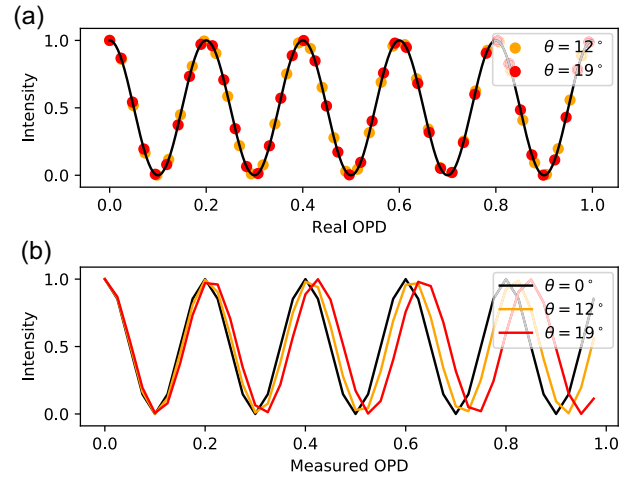

Figure A2. Effect of the incident angle θ on the sampling step size and the measured frequency of an emission line. (a) Positions of the recorded samples of the interferogram of a monochromatic line at two incident angles $12°$ and $19°$ (corresponding roughly to the top and bottom pixels of the FOV). (b) Recorded interferograms at three different incident angles (on-axis and at $12°$ and $19°$). The measured OPD of each sample, which differs from the real OPD, is the on-axis OPD i.e. the target OPD of the mirror controller. The variation of the measured wavelength of the emission line appears clearly.

For the sake of clarity and for future reference, we reproduce here the demonstration of this relation as given in the thesis of Grandmont (2006).

The OPD at any given incident angle is, by definition, the difference between the distance crossed by light in the fixed mirror arm ($D1$) and the moving mirror arm ($2 \times D2$) measured on the wavefront, i.e. perpendicularly to the light direction:

$$OPD = 2 \times D2 - D1. \tag{A3}$$

A superposition of both optical paths is shown in Fig. A1. From simple geometrical consideration, we can deduce that $D2 = \Delta x / \cos(\theta)$, $h = 2 D2 \sin(\theta)$ and $D1 = h \sin(\theta)$ from which it follows that

$$D1 = 2 D2 \sin(\theta)^2. \tag{A4}$$

We can finally write

$$OPD = 2 \frac{\Delta x}{\cos(\theta)} \left(1 - \sin(\theta)^2\right) = 2\Delta x \cos(\theta) = x \cos(\theta). \tag{A5}$$

The effect on the measured wavenumber σ of a single emission line of real wavenumber σ_0 is illustrated in Fig. A2. As the OPD of the light coming with an incident angle is smaller, the interferogram of the source is sampled at shorter steps. If the centroid of the line is calculated considering the step size measured on-axis by the mirror controller the same emission-line will thus see its observed wavenumber increased by a factor $1/\cos(\theta)$ i.e.

$$\sigma = \frac{\sigma_0}{\cos \theta}. \tag{A6}$$

APPENDIX B: EXCERPT FROM THE CATALOGUE

Table B1. Excerpt from the catalogue.

ID	α_{2000}	δ_{2000}	V^a	$\epsilon_V{}^a$	σ^a	$\epsilon_\sigma{}^a$	$F(\mathrm{H}\alpha)^b$	$\epsilon_{F(\mathrm{H}\alpha)}{}^b$	$F([\mathrm{N\,II}]\lambda6584)^b$	$\epsilon_{F([\mathrm{N\,II}]\lambda6584)}{}^b$	$F([\mathrm{S\,II}])^b$	$\epsilon_{F([\mathrm{S\,II}])}{}^b$	Me06^c	Ha06^d	Ma06 H α^e	Ma06 [O III]^e	Comments
S004236.99+411209.3	00 42 36.99	+41 12 09.3	−0595.6	+0002.4	+0032.9	+0001.0	2.35e-15	1.23e-16	1.78e-15	1.00e-16	<4.1e-16	–	2806	P69	Sat.	Sat.	–
S004239.81+411641.5	00 42 39.81	+41 16 41.5	−0175.5	+0002.5	+0020.0	+0001.9	2.30e-15	1.64e-16	1.73e-15	1.41e-16	<6.3e-16	–	–	–	Sat.	Sat.	–
S004241.24+411909.5	00 42 41.24	+41 19 09.5	−0144.7	+0002.7	+0011.6	+0004.1	8.51e-16	7.13e-17	<1.2e-16	–	<2.1e-16	–	802	P105	Sat.	Sat.	–
S004254.20+411336.8	00 42 54.20	+41 13 36.8	−0341.0	+0002.5	+0020.6	+0001.9	1.24e-15	8.20e-17	<2.2e-16	–	<1.5e-16	–	1241	P475	Sat.	Sat.	–
S004242.16+411820.3	00 42 42.16	+41 18 20.3	+0045.4	+0004.2	+0057.4	+0003.6	2.25e-15	2.08e-16	<5.1e-16	–	<2.6e-16	–	–	–	Sat.	Sat.	–
S004229.73+411351.8	00 42 29.73	+41 13 51.8	−0504.5	+0002.3	+0022.4	+0000.8	4.26e-15	1.96e-16	1.55e-15	9.51e-17	<5.0e-16	–	1131	P98	Sat.	Sat.	–
S004254.94+411257.2	00 42 54.94	+41 12 57.2	−0438.5	+0002.3	+0023.1	+0001.0	1.80e-15	9.47e-17	1.48e-15	8.20e-17	<3.2e-16	–	–	–	Sat.	Sat.	–
S004244.51+411813.4	00 42 44.51	+41 18 13.4	−0022.9	+0002.5	+0017.1	+0002.1	1.86e-15	1.24e-16	7.56e-16	8.11e-17	<3.4e-16	–	3029	–	Sat.	Sat.	–
S004302.60+411558.3	00 43 02.60	+41 15 58.3	−0040.2	+0002.3	+0019.4	+0001.2	1.74e-15	9.89e-17	1.79e-15	1.01e-16	<4.1e-16	–	–	–	Sat.	Sat.	–
S004235.97+411410.5	00 42 35.97	+41 14 10.5	−0280.7	+0002.6	+0019.9	+0002.2	1.29e-15	1.04e-16	9.87e-16	9.10e-17	<2.7e-16	–	1205	–	Sat.	Sat.	–
S004257.87+411243.4	00 42 57.87	+41 12 43.4	−0186.2	+0002.3	+0028.1	+0000.9	2.52e-15	1.23e-16	4.86e-16	5.09e-17	<2.3e-16	–	1232	–	Sat.	Sat.	–
S004257.70+411951.0	00 42 57.70	+41 19 51.0	−0324.2	+0002.3	+0016.5	+0001.4	1.69e-15	9.28e-17	1.00e-15	6.69e-17	<2.8e-16	–	809	–	Sat.	Sat.	–
S004239.73+411839.4	00 42 39.73	+41 18 39.4	−0362.3	+0002.4	+0021.1	+0001.4	1.92e-15	1.10e-16	3.83e-16	5.66e-17	<3.2e-16	–	–	–	Sat.	Sat.	–
S004255.48+411721.1	00 42 55.48	+41 17 21.1	−0287.6	+0002.4	+0034.2	+0000.9	3.79e-15	1.97e-16	2.94e-15	1.63e-16	7.61e-16	1.33e-16	1268	P30	Sat.	Sat.	–
S004245.85+411735.4	00 42 45.85	+41 17 35.4	+0020.3	+0002.6	+0022.9	+0002.0	1.75e-15	1.36e-16	1.37e-15	1.20e-16	<6.4e-16	–	1360	–	Sat.	Sat.	–
S004242.48+411356.4	00 42 42.48	+41 13 56.4	−0413.6	+0002.7	+0029.9	+0001.7	1.90e-15	1.36e-16	1.20e-15	1.05e-16	<5.7e-16	–	1246	–	Sat.	Sat.	–
S004231.48+411614.7	00 42 31.48	+41 16 14.7	−0378.7	+0002.6	+0020.1	+0002.2	1.44e-15	1.07e-16	<3.1e-16	–	<2.3e-16	–	1162	–	Sat.	Sat.	–
S004239.57+411831.6	00 42 39.57	+41 18 31.6	−0261.0	+0002.7	+0021.7	+0002.4	1.23e-15	9.74e-17	<2.9e-16	–	<2.4e-16	–	3270	P102	Sat.	Sat.	–
S004235.29+411446.0	00 42 35.29	+41 14 46.0	−0255.4	+0002.3	+0022.3	+0000.9	4.59e-15	2.21e-16	7.73e-16	8.88e-17	<3.2e-16	–	1139	P53	Sat.	Sat.	–
S004246.10+411516.5	00 42 46.10	+41 15 16.5	−0192.7	+0002.9	+0028.3	+0002.1	2.43e-15	1.92e-16	<4.8e-16	–	<1.9e-16	–	1287	–	Sat.	Sat.	–
S004256.13+411632.5	00 42 56.13	+41 16 32.5	−0172.2	+0002.5	+0020.0	+0001.7	1.57e-15	1.10e-16	1.53e-15	1.09e-16	<3.7e-16	–	–	–	Sat.	Sat.	–
S004305.91+411846.0	00 43 05.91	+41 18 46.0	−0550.1	+0002.5	+0020.1	+0001.7	1.38e-15	8.84e-17	7.63e-16	6.43e-17	<2.8e-16	–	–	–	Sat.	Sat.	–
S004232.73+411916.9	00 42 32.73	+41 19 16.9	−0518.7	+0002.3	+0019.3	+0000.9	2.67e-15	1.25e-16	<2.2e-16	–	<2.0e-16	–	2753	–	Sat.	Sat.	–
S004229.58+411404.3	00 42 29.58	+41 14 04.3	−0275.5	+0002.4	+0022.0	+0001.2	2.34e-15	1.26e-16	9.41e-16	7.36e-17	<3.3e-16	–	1132	P50	Sat.	Sat.	–
S004251.86+411214.7	00 42 51.86	+41 12 14.7	−0555.6	+0002.3	+0025.3	+0000.7	3.53e-15	1.58e-16	<2.3e-16	–	<3.4e-16	–	1225	–	Sat.	Sat.	–
S004302.58+412028.3	00 43 02.58	+41 20 28.3	−0257.9	+0002.4	+0020.5	+0001.5	1.35e-15	7.99e-17	4.76e-16	4.77e-17	<1.9e-16	–	2755	P200	Sat.	Sat.	Elongated PSF

Notes. ^{a}Velocity V and broadening σ are expressed in km s^{-1}. The uncertainties are, respectively, ϵ_V and ϵ_σ.
^{b}Fluxes are expressed in erg cm^{-2} s^{-1}. The uncertainties are represented with the letter ϵ. In the case of [S II], the reported flux is the sum of [S II]$\lambda6717$ and [S II]$\lambda6731$; in most cases only an upper limit can be given.
^{c}Index of the cross-matched source of Merrett et al. (2006).
^{d}Index of the cross-matched source of Halliday et al. (2006).
^{e}Index of the cross-matched source of Massey et al. (2006) in the [O III]/B frame or the H α/R frame (see the text for details). (T) indicates a detection; (Sat.) indicates a saturated region.

This paper has been typeset from a TeX/LaTeX file prepared by the author.